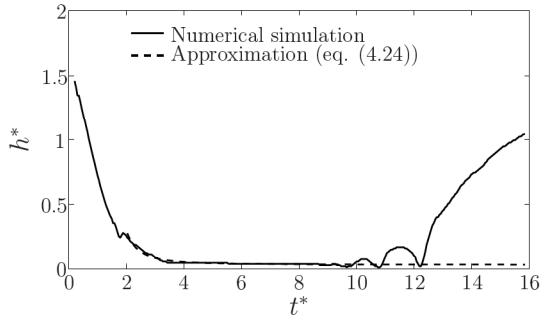


(a) Distilled water, $h^* = 0.5$, $We = 111$, $Re = 4,871$

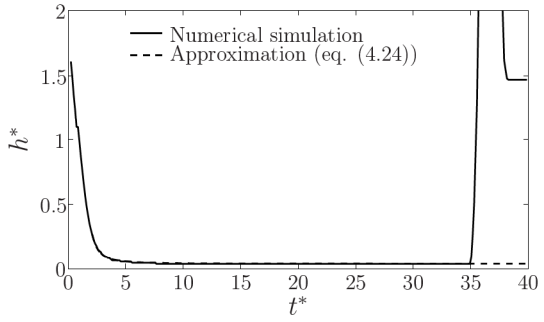


(b) Isopropanol, $h^* = 0.5$, $We = 541$, $Re = 2,007$

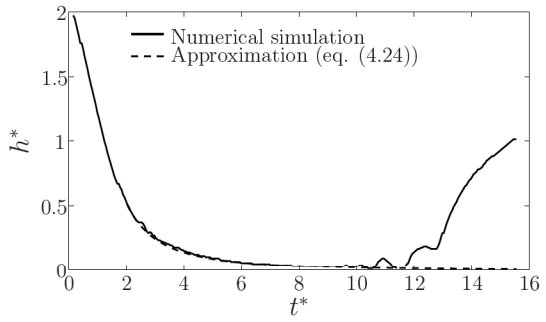


(c) Distilled water, $h^* = 1.0$, $We = 105$, $Re = 4,744$

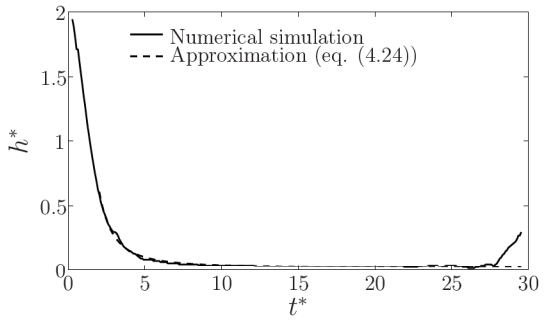


(d) Distilled water, $h^* = 1,0$, $We = 328$, $Re = 8,342$

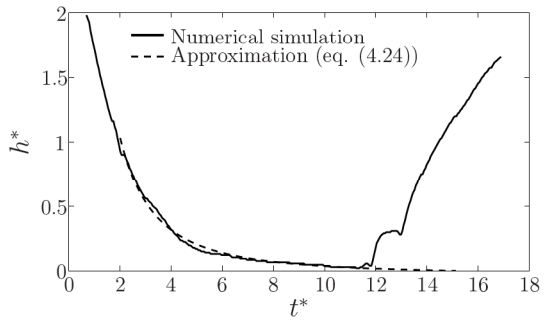


(e) Distilled water, $h^* = 1.5$, $We = 110$, $Re = 4,870$

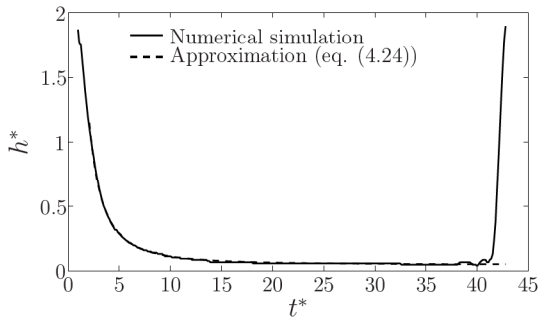


(f) Isopropanol, $h^* = 1.5$, $We = 535$, $Re = 2,006$

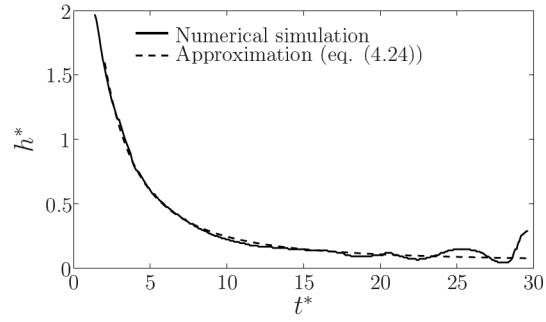


(g) Distilled water, $h^* = 2.0$, $We = 345$, $Re = 8,644$

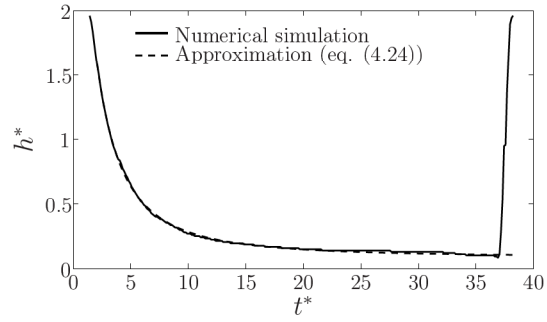


(h) Glycerine/water, $h^* = 2.0$, $We = 505$, $Re = 561$

Figure 4.30: Evolution of the film thickness present below the cavity for different liquids, initial surface film thicknesses and Weber numbers

shown. It can be seen that the theoretical equation approximates the residual film thickness very well for each of the investigated initial liquid film thicknesses. The main trend for each curve is a decrease of the values for $h^*_{res}$ with increasing Reynolds number. For each curve an asymptotic value of the residual film thickness is observed for very high Reynolds numbers, its value increasing for higher initial liquid film thicknesses (Figure 4.31(b)). For $h^* = 2.0$ some scatter in the minimum residual film thickness is observed. The reason for this scatter is that an initial film thickness of $h^* = 2.0$ lies already in the region of deep pools, where the interaction of the cavity with the bottom of the liquid film is less, since the cavity does not always near the bottom of the liquid film as close as for the other investigated initial liquid films due to the higher surface tension forces acting on the expanding cavity (compare, for example, the Figures 4.30(a) to 4.30(f) for $h^* = 0.5$ to $h^* = 1.5$ with the Figures 4.30(g) and 4.30(h) for $h^* = 2.0$).

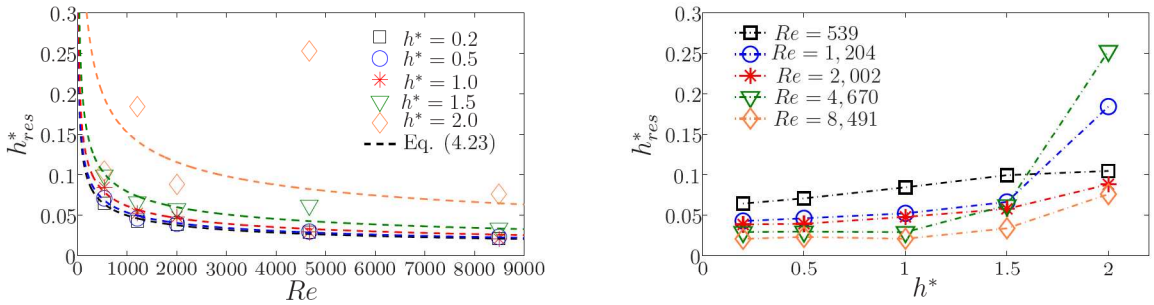


(a) Dependency $h_{res}$ on $Re$

(b) Dependency $h_{res}$ on $h^*$

Figure 4.31: Evolution of minimum residual liquid film thickness as function of $Re$ (left) and $h^*$ (right). Comparison of approximated residual liquid film thickness (symbols) with analytical approximation (dashed lines)

## 4.6 Summary

In this chapter the results of the single drop impingement measurements onto a steady liquid surface film of finite thickness have been presented in detail. The presentation of the results was split up into four main parts, each of which focussed on both the depth or diameter evolution of the cavity in time after drop impingement. The first part focussed on the observations of the cavity dynamics in time by means of shadowgraph recordings. The influence of several drop and film parameters was explained, where the emphasis was put on the qualitative analysis of the data. The second part explained the results of the time evolution of the diameter of the cavity for the complete impingement process, hence from the first moment of impingement until the central jet is formed after the cavity has retracted. In this section the theoretical models were derived and compared with the experimental and numerical results. The differences in the cavity evolution for a change in the initial liquid surface film thickness, in Weber number of the impinging drop and in the liquid properties (surface tension and viscosity) were described and analysed. The third part of this chapter focussed on the time evolution of the depth of the cavity for the complete impingement process. Just like for the diameter evolution also here the differences in the cavity evolution for a change in the initial liquid surface film thickness, in Weber number of the impinging drop and in the liquid properties (surface tension and viscosity) were described and analysed. The final part of this chapter focussed on the time evolution of

the thickness of the initial liquid film, in particular on the minimum value of the thickness of the residual liquid surface film. Hereafter, only the most important observations and results will be summarised.

In this chapter the observations of the single drop impingements onto steady liquid surface films have been presented and used for a detailed qualitative analysis. The main accent was put on the time change of the cavity upon impingement onto a steady liquid film of finite thickness for the complete impingement process, hence from the first moment of impingement until the central jet is formed after the cavity has retracted. The differences in the cavity evolution for a change in the initial liquid surface film thickness, in Weber number of the impinging drop and in the liquid properties (surface tension and viscosity) were described and analysed.

Based on the observations the single drop impingement process can generally be divided into eight different phases:

i characterisation of the drop and liquid surface topology just before impingement;

ii appearance of the prompt splash and initial deformation of the drop;

iii formation of the cavity below the liquid surface;

iv expansion of the cavity to its maximum radial position;

v appearance of the capillary waves;

vi receding and merging of the cavity;

vii retraction of the cavity and emergence of the Worthington jet;

viii formation and impingement of secondary droplets.

For the single drop impingement onto a steady liquid film of finite thickness a change in thickness of the liquid film results in a clear change of the shape of the cavity upon impingement. The corona, formed above the liquid surface upon impingement, is seen to be more pronounced and unstable for thin liquid films. Since the penetration velocity of the cavity is constant for all investigated parameters, a change in film thickness by constant Weber numbers of the impinging drops results for thin surface films in an oblate cavity with a large value for the maximum diameter, whereas for larger film thicknesses the cavity is hemispherical.

An increase in the Weber number of the impinging drop, hence the terminal velocity of the drop upon impingement, leads to a stronger prompt splash, in combination with a higher and unstable corona and a cavity with a larger maximum diameter. The velocity with which the cavity penetrates into the liquid film is independent of the Weber number. The surface tension forces acting on the cavity are weaker for lower Weber numbers, leading to an earlier receding and retraction of the cavity, as well as a thicker and lower central jet.

A change in the liquid properties, hence viscosity and surface tension, has only a clear effect on the time evolution of the cavity during the receding and retraction phases of the impingement process. For a lower value of the surface tension the capillary waves, generated by a sudden increase in pressure at the top of the cavity as a result of the mergence of the plunging rim with the liquid film, are more pronounced and the receding and retraction phases start later and continue during a longer time.

Based on these observations the emphasis was put on the evolution of the diameter of the

cavity and the depth of the cavity in time to be able to compare the different impingement outcomes not only qualitatively, but also quantitatively. In each of the three main parts of this chapter the experimental results have been compared with the analytical models and the results of the numerical simulations. For the single drop impingement onto steady liquid films two kinds of numerical simulations have been done: simulations having an axi-symmetrical grid, defined as a slice of a cylinder having an opening angle of 5° with only one cell in the azimuthal direction, and three-dimensional simulations. It has been shown that the differences between axi-symmetrical simulations and fully three-dimensional simulations are only minor and focus mainly on the receding phase of the cavity. Due to the three-dimensional simulation of the impingement process, the flow of the rim could be solved in a three-dimensional way, resulting in a lower curvature of the capillary wave during the receding phase. This led to a lower pressure difference between the leading and the trailing edge of the capillary wave and thus a lower vertical wave velocity. The subsequent receding of the cavity took longer and the retraction of the cavity was later, which led to a better correlation between the experimental data and the numerical simulations. However, here the results of the axi-symmetrical numerical simulations were used to be compared with the experimental data, since most of the simulations were done with an axi-symmetrical grid and the minor differences between the two kinds of simulations did not lead to large errors in the analysis of the time evolution of the cavity.

For the initial phase of the impingement process a good correlation could be seen between the experimental data of the depth evolution of the cavity in time and the analytical approximation ($y^*_{cav} \sim t^{*2/5}$) for the first non-dimensional time instants after impingement. For larger non-dimensional times a deviation was found between the experiments and the theory, due to the vicinity of the cavity tip to the bottom of the film. This deviation grew with time and increased faster for lower values of the initial surface film thickness. For the time evolution of the diameter at the initial phase after impingement it was found that the remote asymptotic solution, derived by Yarin and Weiss [196] for single drop impingement onto deep pools ($D^{*2}_{cr} \sim t^*$), correlated well with the experimental data. Also here a deviation between the experimental data and the theory was observed for larger time instants, since the theoretical description did not account for the influence of the surface tension, gravity and the interaction of the expanding cavity with the bottom of the liquid film, which are important factors for describing the process of the single drop impingement onto thin liquid films.

The results for the depth and diameter evolution of the cavity in time for the complete impingement process showed several interesting phenomena when comparing the results for different initial liquid film heights, drop impingement Weber numbers and liquids. First of all, due to the high impingement Reynolds numbers the influence of the viscosity could be neglected in the impingement process. Secondly, the numerical simulations correlated very well with the experimental data, both for the time evolution of the cavity depth and of the cavity diameter.

For the time evolution of the depth of the cavity it was observed that the velocity with which the cavity penetrated into the liquid film was constant, hence independent of all the investigated parameters, and equalled $U^*_{cav} = 0.5$. The time at which the cavity reached its maximum depth was dependent on the initial liquid film thickness, being larger for larger initial film thicknesses. The behaviour was not linear, as would be expected for a constant penetration velocity of the cavity, due to the larger expanded cavity and subsequent higher surface tension forces for thicker surface films. Furthermore it was observed that the time at which the cavity started its retraction phase was independent of the surface film thickness, but correlated linearly with the Weber number of the impinging drop and the surface tension of the liquid. A higher Weber

number led to a later retraction of the cavity, since surface tension forces could be overcome for a longer time by inertia. The same behaviour was found for a lower value of the surface tension, where the surface tension forces, responsible for the retraction of the cavity, were lower.

The analytical models, based on the propagation of a kinematic discontinuity (Yarin and Weiss [196]) and describing the time evolution of the cavity diameter, the maximum cavity diameter and the time this maximum cavity diameter is reached, predicted the experimental data very well and could be used to model the time evolution of the diameter of the cavity very accurately. Looking at the influence of the investigated parameters on the diameter evolution of the cavity in time, it was observed that an impingement upon a thicker surface film resulted in a lower expansion of the cavity, due to the larger surface tension forces and the effect of gravity that had to be overcome. The same effect was seen for lower Weber numbers of the impinging drops, hence less available inertia to overcome the surface tension forces, and for liquids with higher surface tensions, due to which the surface tension forces, opposing the expansion of the cavity, were higher.

The non-dimensional time instant at which the maximum diameter of the cavity was reached, was independent of the initial thickness of the liquid surface film, but depended linearly on the Weber number of the impinging drop and on the surface tension of the liquid. For a higher value of the Weber number and for a lower value of the surface tension, the maximum diameter was reached later, since inertia could overcome the surface tension forces easier and for a longer time. The corresponding value of the maximum diameter of the cavity was subsequently larger for higher Weber numbers and lower values of the surface tension. The decrease of the cavity diameter during the receding phase of the impingement process was not influenced by the thickness of the initial surface film. A lower value of the surface tension of the liquid, however, led to a longer period during which the receding took place, whereas a lower Weber number resulted in a faster receding and retraction of the cavity.

With the use of the results of the numerical simulations the time evolution of the residual film thickness could be analysed. It was found that the theoretical approximations, derived in §(4.5.1), described the time evolution of the residual film thickness very accurately until the moment the cavity started to collapse. By applying these analytical models the minimum value of the residual liquid film thickness could be derived. It was found that the minimum residual film thickness was directly related to the Reynolds number of the impinging drop and could be described by $h^*_{res} \sim Re^{-2/5}$. For very high Reynolds numbers the asymptotic value of the minimum residual film thickness increased with increasing thickness of the initial surface film.

In the following chapter of Part I of this thesis the results of the single drop impingement onto wavy liquid surface films will be discussed and compared with the results of the steady impingement, in order to show that not only the waviness of the liquid film, but also the velocity and amplitude of the surface film, have a significant influence on the drop impingement outcomes and thus also on the spray impingement process.

# Chapter 5

# Dynamics of cavity evolution for drop impingements onto wavy liquid films

The complete process of the single drop impingement onto steady liquid films of finite thickness has been analysed in Chapter 4. In that chapter the focus was put on the evolution of the cavity in time from the time instant at which the impinging drop made first contact with the surface film to the moment the central jet had been formed. In particular the emphasis was laid on the time change of the depth of the cavity, hence its lowest point, and the diameter of the cavity at half its maximum depth. A comparison of the experimentally obtained data with the numerical simulations and the analytical models was made for the impingement outcomes by varying the most important drop and film parameters. It was shown that the obtained theoretical models and numerical simulations predicted the impingement processes to a very high degree.

These analytical models, based on the experimental data obtained for single drop impingements upon steady liquid surface films, are commonly used for the modeling of spray impingement processes by applying the superposition principle. This means that the impingement of each drop inside the spray is modeled individually by assuming that no other drops are present within a certain boundary around the impingement area; hence the impingement of each single drop of the spray is not influenced by other surrounding drop impingements. Several studies, however, have shown that this superposition principle cannot be used for describing the spray impingement process statistically. Sprays are a collection of a large number of drops, where the outcome of each individual drop impingement onto a liquid film is influenced by the unsteady wall film flow generated by the surrounding impingements, as well as by the interactions with other impinging drops, both in the spray and during the interaction with the wall film. All of these factors have a significant effect on the spray impingement process, thereby drastically changing the mathematical description of the spray impingement.

This will be verified in the first part of this chapter, where a comparison will be made between the observations of the single drop impingement studies onto steady liquid surface films and solitary surface waves, by means of Shadowgraph recordings. In order to investigate the behaviour of the cavity appearing after drop impingement onto a wavy liquid surface, a solitary surface wave is generated. The influence of the amplitude and velocity of this wave on the drop impingement outcome will be shown, as well as the influence of the phase of the wave at which the drop impinges. To study the influence of the impinging drop Weber number on the cavity evolution in time the terminal velocity of the drop before impingement $U_d$ is changed. Just as for the single drop impingement measurements onto a steady liquid surface, the influence of

the viscosity of the liquid is investigated for the impingements onto solitary surface waves. The liquid film height, however, is kept constant for these measurements. For each of the different investigated parameters two comparative measurements are conducted and will be shown herefater: the impingement of a single drop onto a steady liquid film and the measurement of the wave without an impinging drop. The first measurement is used as a reference measurement to compare directly the changes in the cavity evolution with and without a solitary surface wave, whereas the second measurement is needed to measure the exact behaviour of the wave, hence, the velocity and amplitude evolution of the wave in time.

In the second part of this chapter the impingement outcomes, in particular the time evolution of the cavities formed after the impingement onto standing waves and solitary surface waves, will be analysed in more detail. The evolution of the depth of the cavity, by measuring its lowest point, will be analysed and compared for different drop impingement parameters and surface film topologies. For the impingements onto solitary surface waves these parameters are the phase of the solitary wave at impingement, the amplification of the wave, hence its velocity and maximum amplitude, the absolute Weber number of the impinging drop and the liquid properties, whereas for the impingements onto standing waves only the Weber number of the impinging drop is varied. The same analysis will be conducted on the diameter evolution of the cavity at half its maximum depth, in order to investigate the maximum cavity diameter and the time at which this maximum diameter is reached. These results will be compared with the impingement data obtained for the impingements onto steady liquid surface films with the same film thickness.

Table 5.1: Parameters of the selected experiments used for discussion of the outcomes of a drop impingement onto a solitary surface wave

| **Liquid** | **Amplification** | **Phase** | **We** | **Fr** | **Re** | $h^*_{steady}$ |
|---|---|---|---|---|---|---|
| Glycerine/Water | Yes | 58° | 413 | 443 | 10,944 | 6.4 |
| Glycerine/Water | Yes | 144° | 333 | 361 | 9,813 | 6.4 |
| Water | No | 61° | 374 | 313 | 11,080 | 5.8 |
| Water | No | 149° | 374 | 317 | 11,057 | 5.8 |
| Water | Yes | 1° | 335 | 346 | 9,947 | 5.8 |
| Water | Yes | 21° | 331 | 349 | 9,845 | 5.8 |
| Water | Yes | 60° | 354 | 339 | 10,421 | 5.8 |
| Water | Yes | 60° | 256 | 282 | 8,552 | 5.8 |
| Water | Yes | 65° | 392 | 387 | 10,898 | 5.8 |
| Water | Yes | 125° | 352 | 351 | 10,299 | 5.8 |
| Water | Yes | 147° | 342 | 348 | 10,093 | 5.8 |
| Water | Yes | 149° | 293 | 306 | 9,281 | 5.8 |
| | | | | | | |
| Glycerine/Water | - | - | 339 | 367 | 9,883 | 6.4 |
| Water | - | - | 296 | 302 | 9,397 | 5.8 |
| Water | - | - | 353 | 388 | 10,063 | 5.8 |
| Water | - | - | 381 | 406 | 10,539 | 5.8 |
| Water | - | - | 382 | 269 | 11,703 | 5.8 |

## 5.1 Single drop impingement onto solitary surface waves

In §(4.1) the observations of the single drop impingement onto steady liquid films of finite thickness have been presented. The outcomes of the experimental single drop impingement investigations are commonly used as a model to describe the behaviour of spray impingement onto a thin liquid film. However, due to the many interactions taking place between the impinging drops, as well as the rapidly changing topology of the liquid surface film, these models are misleading. Therefore it is obvious that experimental data have to be gathered concerning the influence of the waviness of the liquid surface film during single drop impingement, in order to model the spray impingement processes in a more realistic way.

In this paragraph the observations of the single drop impingement onto a solitary liquid surface wave are presented. For the parametric studies different properties of the impinging drop, which influence the impingement outcomes, and of the solitary liquid surface waves are changed, in order to investigate their influences on the cavity behaviour in time. These parameters are the Weber number of the impinging drop, hence, the terminal velocity of the drop before impingement - since the surface tension is kept unchanged -, the phase of the solitary wave at which the drop impinges, the amplitude and velocity of the solitary wave and the liquid properties (viscosity and surface tension). Seventeen of the many impingement experiments are selected and presented hereafter. The impingement parameters of these experiments are given in Table 5.1. It has to be noted that all notifications hereafter of the Reynolds numbers, Weber numbers and Froude numbers are based upon the absolute impingement velocity, hence the modulus of the vector sum of the velocity vector of the impinging drop and of the solitary surface wave.

### 5.1.1 Evolution of the cavity in time

In Figure 5.1 the evolution of the cavity, appearing after impingement of a distilled water drop onto a solitary liquid surface wave of a deep pool of distilled water of thickness $h^* = 5.8$ is presented at various non-dimensional times. The drop impinges at the wave-phase of $\varphi = 60°$, hence at the leading edge of the surface wave. Here, the leading edge is defined for $0° \leq \varphi \leq 90°$ and the trailing edge for $90° \leq \varphi \leq 180°$, where $\varphi = 0°$ is point at which the wave amplitude equals zero. In this figure, as well as in all the figures presented hereafter, $t^* = 0$ corresponds to the time at which the impinging drop has first contact with the liquid film, whereas the red dashed line is the surface of the solitary wave. A comparison is made with the time evolution of the cavity for a distilled water drop impingement onto a steady liquid surface film of thickness $h^* = 5.8$ (Figure 5.2) to indicate precisely the influences of the propagation of the film surface and the velocity distribution of the film on the cavity after impingement.

In §4.1.1 the mechanism of the drop impingement process onto a steady liquid layer of finite thickness was described by dividing the time evolution of the cavity into several phases. In both of the figures shown below the same eight impingement phases can be found, albeit, depending on the nature of the liquid surface, for different time instants after the drop impingement.

For the impingement onto a steady liquid film and onto a solitary surface wave the following subdivision into the eight different impingement phases can be made:

i Formation and characterisation of the traveling wave, Figure 5.1(a) to 5.1(c). The formation of the wave takes place at the right side of the recordings, due to which the solitary surface wave travels from the right to the left in the images.

(a) $t^* = -27.6$ (b) $t^* = -15.5$ (c) $t^* = -8.2$ (d) $t^* = -1.5$ (e) $t^* = 1.5$

(f) $t^* = 4.4$ (g) $t^* = 8.2$ (h) $t^* = 12.3$ (i) $t^* = 17.4$ (j) $t^* = 20.3$

(k) $t^* = 23.2$ (l) $t^* = 25.6$ (m) $t^* = 28.3$ (n) $t^* = 30.5$ (o) $t^* = 32.9$

(p) $t^* = 34.8$ (q) $t^* = 36.8$ (r) $t^* = 45.0$ (s) $t^* = 52.2$ (t) $t^* = 71.1$

Figure 5.1: Single drop impingement onto a solitary wave. The evolution of the cavity formed by a distilled water drop ($We = 354$, $Fr = 339$, $Re = 10,421$) impingement at various non-dimensional time instants. The impingement parameters are $D_d = 2.9$ mm, $U_d = 2.7$ m/s, $U_w = 0.4$ m/s and $\varphi = 60°$

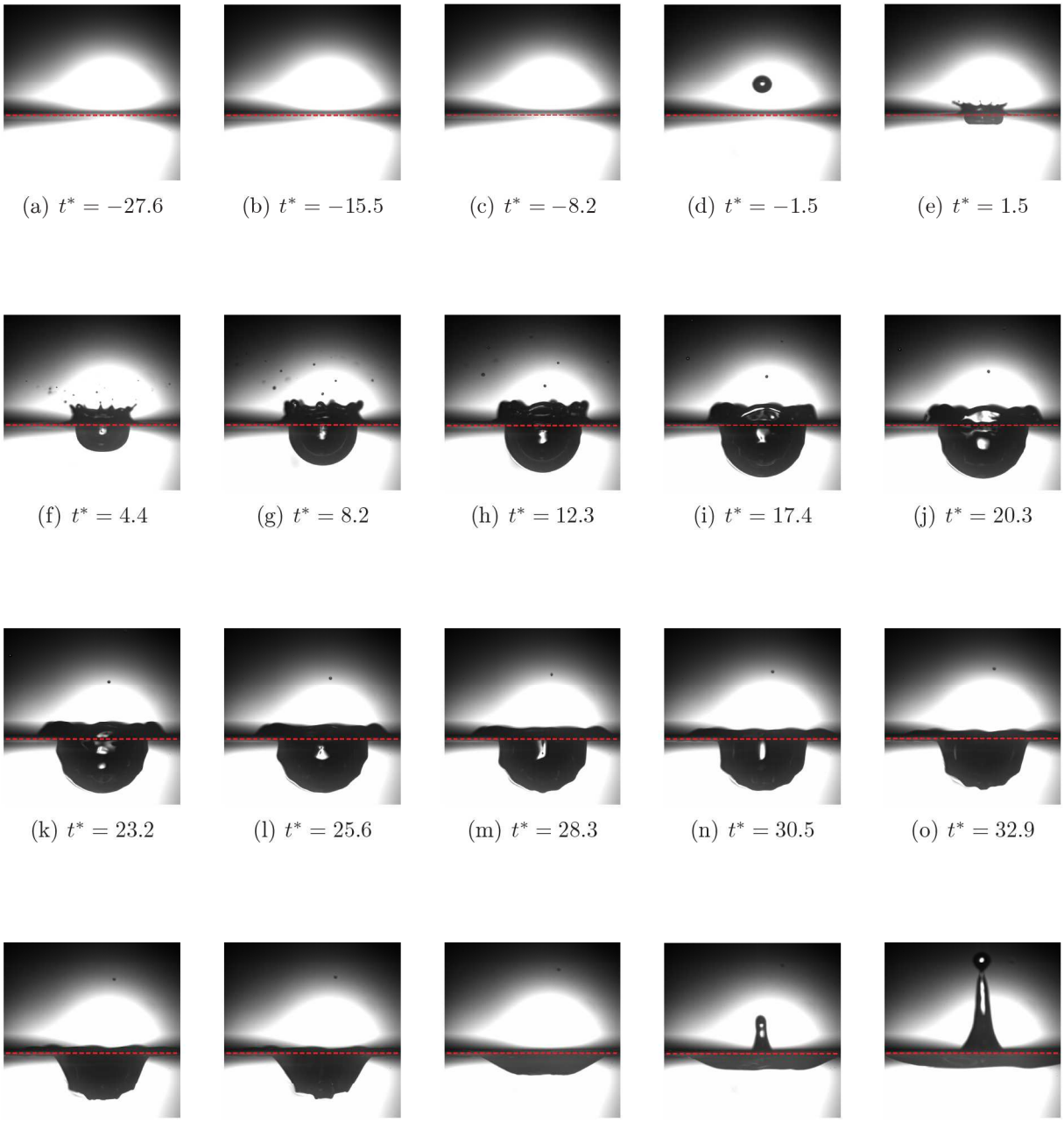

(a) $t^* = -27.6$ (b) $t^* = -15.5$ (c) $t^* = -8.2$ (d) $t^* = -1.5$ (e) $t^* = 1.5$

(f) $t^* = 4.4$ (g) $t^* = 8.2$ (h) $t^* = 12.3$ (i) $t^* = 17.4$ (j) $t^* = 20.3$

(k) $t^* = 23.2$ (l) $t^* = 25.6$ (m) $t^* = 28.3$ (n) $t^* = 30.5$ (o) $t^* = 32.9$

(p) $t^* = 34.8$ (q) $t^* = 36.8$ (r) $t^* = 45.0$ (s) $t^* = 52.2$ (t) $t^* = 71.1$

Figure 5.2: Single drop impingement onto a steady liquid layer of non-dimensional thickness $h^* = 5.8$. The evolution of the cavity formed by a distilled water drop ($We = 353$, $Fr = 338$, $Re = 10,063$) impingement at various non-dimensional time instants. The impingement parameters are $D_d = 2.9$ mm and $U_d = 2.7$ m/s

ii Drop impingement onto the surface of the liquid film and its initial deformation, Figure 5.1(d) (solitary wave) and Figure 5.2(d) and 5.2(e) (steady liquid film). In Figure 5.1(d) it is observed that, since the drop impinges at a wave-phase of $\varphi = 60°$, the absolute liquid pool depth changes from $h^* = 5.8$ to $h^* = 7.4$. Furthermore, one has to take into account that the solitary wave has a relative horizontal velocity ($U_w = 0.39$ m/s) with respect to the impinging drop ($U_d = 2.73$ m/s), due to which the absolute velocity of the drop at impingement equals $U_{d,abs} = 2.75$ m/s.

iii Prompt splash, Figure 5.1(e) (solitary wave) and Figure 5.2(e) (steady liquid film). In these figures it can be seen that the prompt splash mechanism leads to the almost immediate formation of very small jets and secondary droplets. Since the solitary wave moves to the left, it is to be expected that the prompt splash is more vigourous in that direction. The absolute impingement velocity vector is inclined to the left, due to which the kinetic energy is more distributed into this direction, directly leading to a left-directed prompt splash.

iv Formation of a cavity, Figure 5.1(f) (solitary wave) and Figure 5.2(f) (steady liquid film). For the impingement onto a steady liquid film it is seen that the formation of the cavity is symmetrical, whereas the solitary wave clearly changes the formation process. Due to the left-directed absolute velocity of the solitary surface wave the top of the cavity moves to the left with approximately the solitary wave velocity $U_w$. A combination of this phenomenon with the decreasing horizontal velocity component of the liquid for increasing distance from the liquid surface leads to an additional inclination of the cavity to the left, thereby increasing its inclination angle in time. At the same time the so-called corona is formed above the surface of the liquid film. For the steady impingement case the corona is growing in a symmetrical way, whereas for the impingement onto the solitary wave, a clear asymmetrical corona is formed. This asymmetry can again be subscribed to the inclined absolute velocity vector of the drop at impingement, due to which more kinetic energy is distributed to the left direction. The rim of the corona can become unstable due to three-dimensional oscillations, resulting in the break-up of the rim into finger-like jets and possible secondary droplets.

v Expansion of the cavity, Figures 5.1(g) to 5.1(i) (solitary wave) and Figures 5.2(g) to 5.2(i) (steady liquid film). At these time instants the cavity expands both in diameter as well as in depth, changing the kinetic energy of the impinging drop into surface tension energy and dissipated energy. As has been mentioned before, the cavity in Figure 5.1 expands with increasing inclination, due to the differences in the horizontal velocity components of the film at different distances from the surface. Would the images be rotated at the angle, defined between the inclination of the surface at the point of impingement and the vertical axis, the cavity would look almost perfectly symmetric. This is, however, not applied in this thesis for two reasons. First of all, this would not represent the physical nature of spray impingement, as for spray impingement the single drops of the spray always impinge onto an inclined surface. Secondly, not the investigation of the symmetry of the cavity is the main topic of this research, but the influence of the inclination of the surface at impingement, in combination with the velocity of the liquid film.

vi Appearance of the capillary waves, Figure 5.1(j) (solitary wave) and 5.2(j) (steady liquid film). These rather sharp capillary waves appear on the surface of the cavity. They are created at the inside of the corona at the time instant at which the rim, falling back onto the liquid surface due to gravity, merges with the liquid film. The detailed

description of the capillary waves has been given in §4.1.1. The pressure differences ahead of and behind the capillary waves lead to the liquid acceleration and enhance the wave propagations, due to which the capillary waves move downwards along the cavity surface, thereby accelerating when approaching the bottom of the cavity. For liquids with low surface tensions trains of capillary waves can be observed, see for example Figure 5.2(m), where three capillary waves can be seen. The front capillary waves are usually small in amplitude, whereas the last capillary waves have an increased amplitude and wave velocity.

vii Receding and merging of the cavity, Figures 5.1(k) to 5.1(n) (solitary wave) and Figures 5.2(k) to 5.2(q) (steady liquid film). Due to the surface tension forces acting on the cavity surface, as well as the downward motion of the capillary waves, the cavity changes its shape from a hemisphere to a cone. The capillary waves merge at the bottom of the cavity, leading to a sharp cone angle, where high pressure differences and surface tension forces are present. The receding of the cavity for the steady liquid film impingement takes place in a highly symmetrical way, since the capillary waves have the same shape and penetrate into the liquid film with the same velocity at all azimuthal angles. Additionally, the shape of the cavity itself is highly symmetrical, due to which the surface tension forces, acting on the surface of the cavity, are equally distributed along the cavity. Figure 5.1 clearly shows that the receding of the cavity for the impingement onto a solitary wave is far from symmetrical. First of all, the surface of the cavity at the leading edge of the wave, i.e. the left part of the cavity, is less than at the trailing edge, due to the inclination of the cavity. This results in an unequal distribution of the surface tension forces over the cavity. Second, in Figure 5.1(j) it is seen that at the right side of the cavity a strong capillary wave appears, which travels downwards along the surface of the cavity in the time instants between $20.3 \leq t^* \leq 28.3$. Due to this moving capillary wave the right side of the cavity changes its shape from spherical to a straight line. At the left side of the cavity no capillary wave appears during this time, as a result of which the left cavity surface changes its shape only in a minor way. At approximately $t^* - 30.5$ the right capillary wave has reached the bottom of the cavity and a conical cavity appears with a sharp cone angle. It can therefore be concluded that the receding of the cavity for the impingement onto a solitary wave is directly influenced by the presence and/or absence of the capillary waves at the left and right side of the cavity, in combination with the unequal distribution of the surface tension forces over the cavity surface.

viii Retraction of the cavity and emergence of a central jet, Figures 5.1(o) to 5.1(t) (solitary wave) and Figures 5.2(r) to 5.2(t) (steady liquid film). Due to the high pressure differences and surface tension forces at the bottom of the cavity, the cavity starts its retracting motion. As a result of the velocity with which the center of the cavity moves upwards a central jet is formed. Also for the formation of the central jet a clear difference is seen between the two impingement processes. Due to the symmetrical receding and merging of the cavity for the drop impingement onto the steady liquid film the cavity retracts in a symmetrical way and a straight, central jet is formed. For the impingement onto the solitary wave the receding of the cavity is highly asymmetrical, therefore leading to a clear asymmetrical retraction of the cavity, Figure 5.1(p). This results in a Worthington jet, which is much lower and thicker than is the case for the impingement onto a steady surface film, compare Figure 5.1(s) with Figure 5.2(s). As a result of the asymmetrical receding of the cavity in the case of the impingement onto the solitary wave, the high surface tension forces and pressure differences are not centered in a strong way at one

point, as is the case for the impingement onto a steady liquid film.

It can be summarised that a clear influence on the outcome of the impingement process and on the evolution of the cavity shape in time appears by changing the topology of the liquid surface film. The solitary wave induces a relative velocity component upon impingement, due to which the shape and inclination of the corona are changed. Additionally, as a result of the decreasing horizontal velocity component inside the liquid film with increasing depth, the cavity inclines in the direction of the wave propagation, resulting in an asymmetrical expansion of the cavity during the first stages after impingement. The presence or absence of the capillary waves at the left and right side of the cavity, in combination with the unequal distribution of the surface tension forces over the cavity surface, induce an asymmetrical receding and retraction of the cavity, as well as an inclined Worthington jet.

### 5.1.2 Influence of the wave-phase on the cavity shape

The topology of the surface film during spray impingement is highly transient. The height of the liquid film changes locally at a high frequency, thereby introducing local surface inclinations. Several studies have been conducted to simulate the spray impingement process onto inclined liquid films, by investigating the inclined impingements onto steady liquid films (Schotland [147], Jayaratne and Mason [65], Zhbankova and Kolpakov [201], Leneweit *et al.* [81], Okawa *et al.* [107]). The outcomes of these studies, however, do not represent the physics of spray impingement, since first of all only one single inclined drop impingement is investigated, and secondly the high frequency with which the drops of the spray are impinging onto the surface film induces simultaneously a film velocity. This relative film velocity is not taken into account by the studies of an inclined impingement onto a steady surface film.

In this paragraph the results of the influence of the phase of the wave, hence its inclination, in combination with the relative film motion, on the time evolution of the cavity are presented in the Figures 5.3, 5.4 and 5.5. The impingements onto 11 different phases of the wave, in the range of $\varphi = 1°$ to $\varphi = 180°$, are investigated. This range of phases is taken, since the amplitude of the wave at the second half of the wavelength ($180° \leq \varphi \leq 360°$) is much lower than the amplitude of the first half of the wavelength due to energy dissipation during the propagation of the surface wave. The outcomes of the single drop impingements for distilled water onto five of these wave phases ($\varphi = 1°$, $\varphi = 21°$, $\varphi = 60°$, $\varphi = 125°$ and $\varphi = 147°$) are shown in these figures. For each of these measurements the Weber number, Froude number and Reynolds number of the impinging drops are in the same range. Figure 5.3 shows the drop impingement outcomes inbetween the non-dimensional times $t^* = -1.5$ and $t^* = 12.3$, Figure 5.4 for the non-dimensional times inbetween $t^* = 20.3$ and $t^* = 32.9$ and Figure 5.5 for the non-dimensional times inbetween $t^* = 34.8$ and $t^* = 71.1$.

Right upon impingement, at $t^* = 1.5$, the first interesting differences can be observed. Concerning the prompt splash, which is present for the impingements of all shown phases of the solitary wave, it is found that the shape of the wave has a clear influence on it. In case of impingement onto the leading edge of the wave, hence $\varphi \leq 90°$, the prompt splash is more pronounced in the wave propagation direction. This results in many small jets and secondary droplets being formed at this side of the impingement. At the right side of the forming corona, the prompt splash is less pronounced, since this side of the corona interacts with the leading edge of the wave in such a way that the corona formation is being prohibited. The same can be observed for the cases where the drops impinge onto the trailing edge of the wave, hence $\varphi \geq 90°$, in which cases the left side of the forming corona interacts strongly with the trailing

(a) $t^* = -1.5$ (b) $t^* = -1.5$ (c) $t^* = -1.5$ (d) $t^* = -1.5$ (e) $t^* = -1.5$

(f) $t^* = 1.5$ (g) $t^* = 1.5$ (h) $t^* = 1.5$ (i) $t^* = 1.5$ (j) $t^* = 1.5$

(k) $t^* = 4.4$ (l) $t^* = 4.4$ (m) $t^* = 4.4$ (n) $t^* = 4.4$ (o) $t^* = 4.4$

(p) $t^* = 8.2$ (q) $t^* = 8.2$ (r) $t^* = 8.2$ (s) $t^* = 8.2$ (t) $t^* = 8.2$

(u) $t^* = 12.3$ (v) $t^* = 12.3$ (w) $t^* = 12.3$ (x) $t^* = 12.3$ (y) $t^* = 12.3$

Figure 5.3: Single drop impingement onto different phases of the solitary wave between $\varphi = 1°$ and $\varphi = 147°$. The evolution of the cavity formed by a distilled water drop impingement at non-dimensional time instants between $t^* = -1.5$ and $t^* = 12.3$. The impingement parameters are for all shown phases: $D_d = 2.9$ mm, $U_d = 3.0$ m/s and $U_w = 0.4$ m/s. Outer left: $\varphi = 1°$, $We = 335$, $Fr = 346$, $Re = 9,947$; middle left: $\varphi = 21°$, $We = 331$, $Fr = 349$, $Re = 9,845$; middle: $\varphi = 60°$, $We = 354$, $Fr = 339$, $Re = 10,421$; middle right: $\varphi = 125°$, $We = 352$, $Fr = 351$, $Re = 10,299$; outer right: $\varphi = 147°$, $We = 342$, $Fr = 348$, $Re = 10,093$

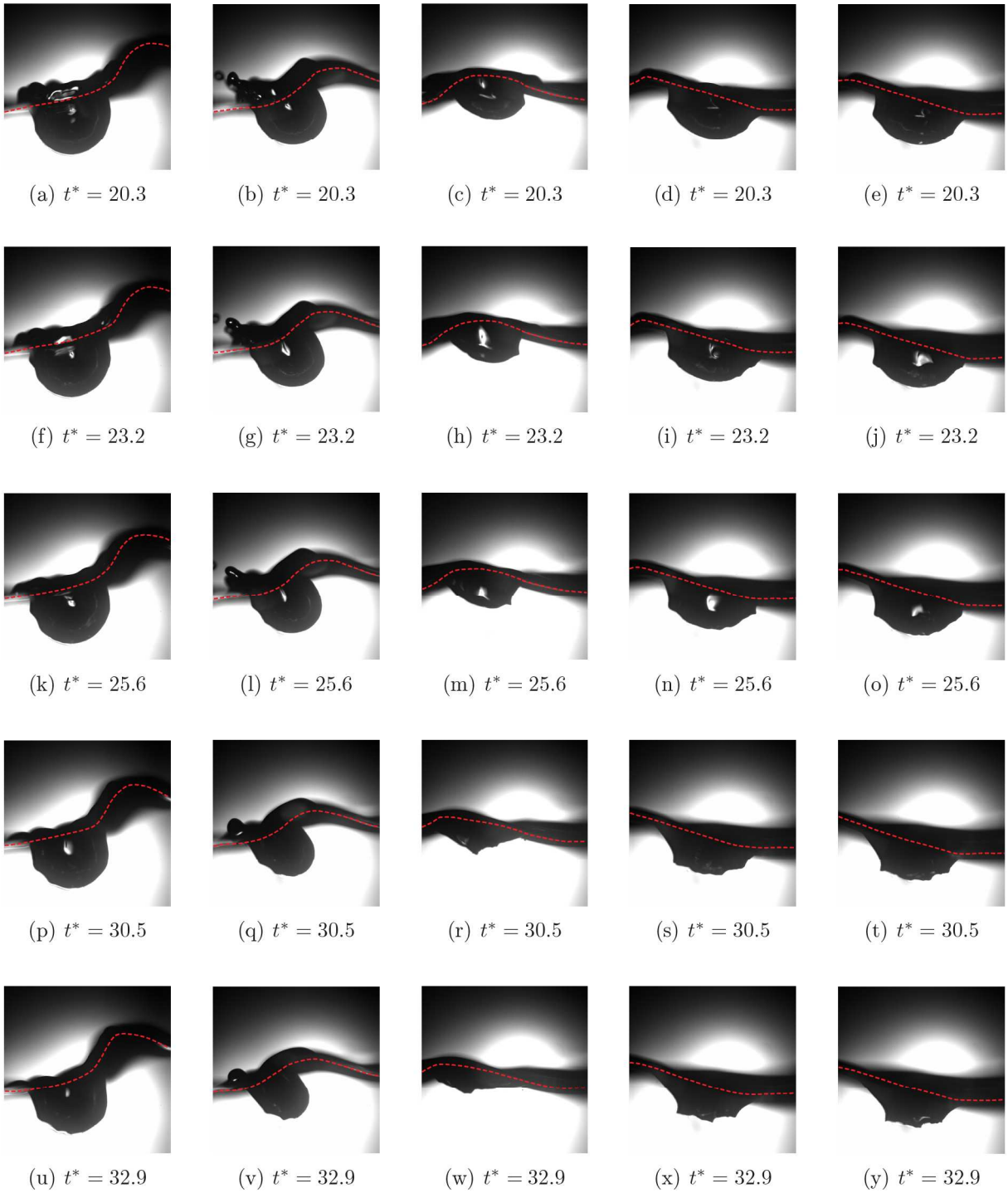

(a) $t^* = 20.3$ (b) $t^* = 20.3$ (c) $t^* = 20.3$ (d) $t^* = 20.3$ (e) $t^* = 20.3$

(f) $t^* = 23.2$ (g) $t^* = 23.2$ (h) $t^* = 23.2$ (i) $t^* = 23.2$ (j) $t^* = 23.2$

(k) $t^* = 25.6$ (l) $t^* = 25.6$ (m) $t^* = 25.6$ (n) $t^* = 25.6$ (o) $t^* = 25.6$

(p) $t^* = 30.5$ (q) $t^* = 30.5$ (r) $t^* = 30.5$ (s) $t^* = 30.5$ (t) $t^* = 30.5$

(u) $t^* = 32.9$ (v) $t^* = 32.9$ (w) $t^* = 32.9$ (x) $t^* = 32.9$ (y) $t^* = 32.9$

Figure 5.4: Single drop impingement onto different phases of the solitary wave between $\varphi = 1°$ and $\varphi = 147°$. The evolution of the cavity formed by a distilled water drop impingement at non-dimensional time instants between $t^* = 20.3$ and $t^* = 32.9$. The impingement parameters are for all shown phases: $D_d = 2.9$ mm, $U_d = 3.0$ m/s and $U_w = 0.4$ m/s. Outer left: $\varphi = 1°$, $We = 335$, $Fr = 346$, $Re = 9,947$; middle left: $\varphi = 21°$, $We = 331$, $Fr = 349$, $Re = 9,845$; middle: $\varphi = 60°$, $We = 354$, $Fr = 339$, $Re = 10,421$; middle right: $\varphi = 125°$, $We = 352$, $Fr = 351$, $Re = 10,299$; outer right: $\varphi = 147°$, $We = 342$, $Fr = 348$, $Re = 10,093$

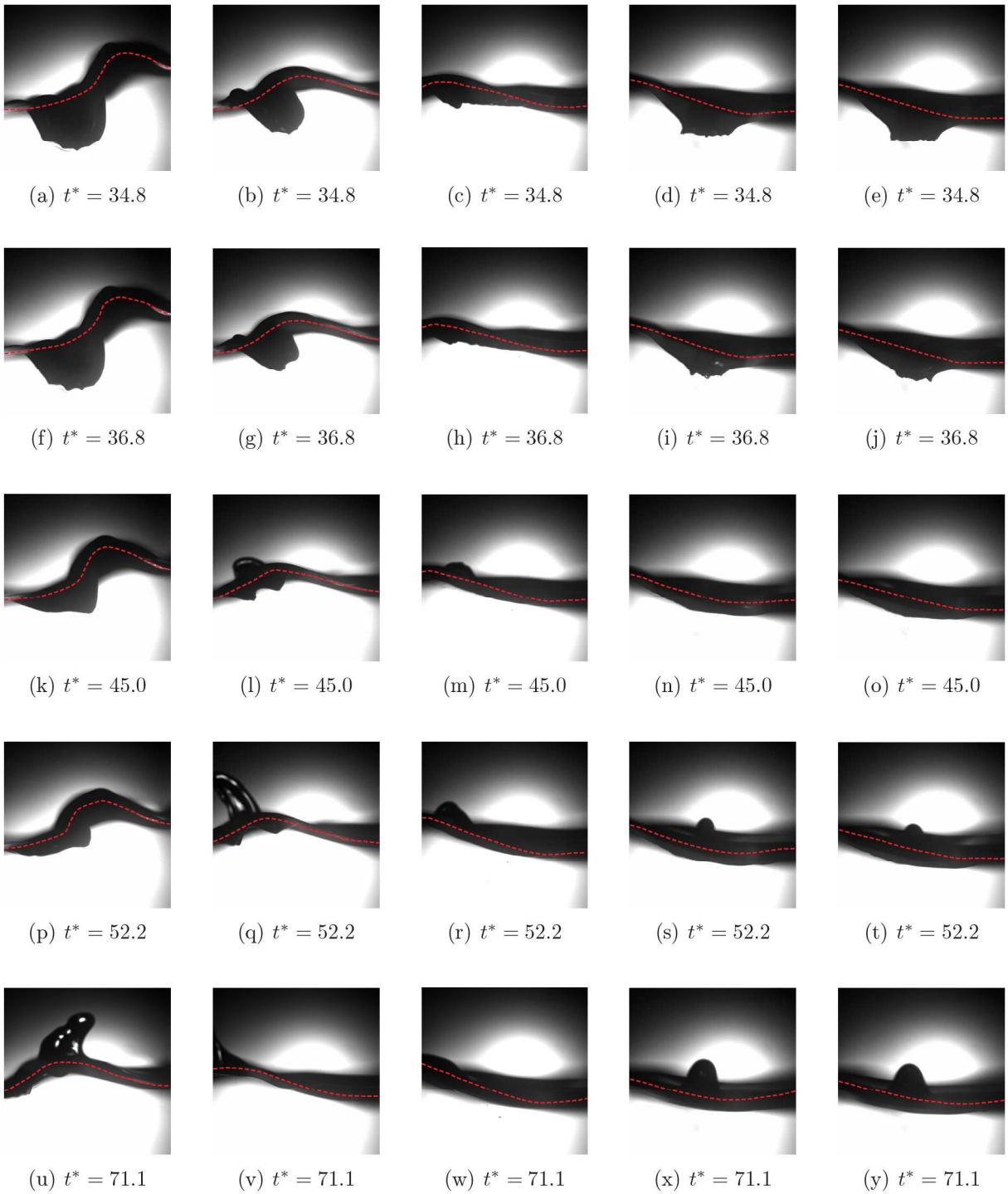

(a) $t^* = 34.8$ (b) $t^* = 34.8$ (c) $t^* = 34.8$ (d) $t^* = 34.8$ (e) $t^* = 34.8$

(f) $t^* = 36.8$ (g) $t^* = 36.8$ (h) $t^* = 36.8$ (i) $t^* = 36.8$ (j) $t^* = 36.8$

(k) $t^* = 45.0$ (l) $t^* = 45.0$ (m) $t^* = 45.0$ (n) $t^* = 45.0$ (o) $t^* = 45.0$

(p) $t^* = 52.2$ (q) $t^* = 52.2$ (r) $t^* = 52.2$ (s) $t^* = 52.2$ (t) $t^* = 52.2$

(u) $t^* = 71.1$ (v) $t^* = 71.1$ (w) $t^* = 71.1$ (x) $t^* = 71.1$ (y) $t^* = 71.1$

Figure 5.5: Single drop impingement onto different phases of the solitary wave between $\varphi = 1°$ and $\varphi = 147°$. The evolution of the cavity formed by a distilled water drop impingement at non-dimensional time instants between $t^* = 34.8$ and $t^* = 71.1$. The impingement parameters are for all shown phases: $D_d = 2.9$ mm, $U_d = 3.0$ m/s and $U_w = 0.4$ m/s. Outer left: $\varphi = 1°$, $We = 335$, $Fr = 346$, $Re = 9,947$; middle left: $\varphi = 21°$, $We = 331$, $Fr = 349$, $Re = 9,845$; middle: $\varphi = 60°$, $We = 354$, $Fr = 339$, $Re = 10,421$; middle right: $\varphi = 125°$, $We = 352$, $Fr = 351$, $Re = 10,299$; outer right: $\varphi = 147°$, $We = 342$, $Fr = 348$, $Re = 10,093$

edge of the wave. This results in a more pronounced prompt splash in the opposing direction of wave propagation, leading to a clear secondary droplet formation at this side of the corona. For $\varphi = 60°$ the prompt splash is seen to be most vigourous, as the drop impinges onto the upper leading part of the wave.

In the next time instants it is observed that not only the prompt splash is strongly influenced by the solitary surface wave, but also a clear interaction of the expanding coronas with the leading or trailing edge of the surface waves is seen to occur. For $\varphi = 1°$, $\varphi = 125°$ and $\varphi = 147°$ the coronas are formed in an approximately symmetrical way, where for the lowest wave-phase the expansion of the corona is more pronounced in the wave propagation direction and for the two highest wave-phases the corona can grow more in the opposing direction. A clear asymmetrical corona formation occurs for $\varphi = 21°$, which is to be expected, since for this phase the interaction with the leading edge of the surface wave is the highest. The growing of the corona for the impingement at $\varphi = 60°$ is only partly influenced by the solitary surface wave, as the right side of the corona can expand over the top of the wave.

At the same non-dimensional time instants ($t^* = 4.4$) the cavities are formed below the liquid surfaces and continue to increase in radial direction. For $\varphi = 1°$, $\varphi = 125°$ and $\varphi = 147°$ the cavities expand symmetrically with respect to the vertical impingement axis. However, for $\varphi = 21°$ and $\varphi = 60°$ the cavity expands in an asymmetrical way. As has been mentioned already in §5.1.1 the top of the cavity moves to the left with approximately the solitary wave velocity $U_w$ due to the left-directed absolute velocity of the solitary surface film. This, in combination with the decreasing horizontal velocity component of the liquid for increasing distance from the liquid surface, results in the additional inclination of the cavity to the left, thereby increasing its inclination angle in time, compare for example Figure 5.3(v) with Figure 5.3(l). The radial expansion of the cavity continues until all the kinetic energy of the impinging drop has been converted into surface tension energy and dissipated energy. The time instants at which this point is reached depend strongly on the phase of the solitary surface wave at impingement, being $t^* = 12.3$ for $\varphi = 147°$, $t^* = 17.4$ for $\varphi = 125°$ and $\varphi = 60°$, $t^* = 20.3$ for $\varphi = 21°$ and $t^* = 23.2$ for $\varphi = 1°$. Clearly, for higher phases of the wave at which the drop impinges, a faster conversion of the kinetic energy takes place.

Around these time instants the capillary waves appear and start their motion downwards along the surfaces of the cavities, thereby changing the shapes of the cavities downstream of the capillary waves. The capillary waves are formed at the time instant at which the rim, falling back onto the liquid surface film due to gravity, merges with the liquid film, thereby generating a strong elevation of the pressure at the top of the cavity. For $\varphi = 147°$ the strong capillary wave appears at $t^* = 12.3$ only at the left side of the cavity, Figure 5.3(y), whereas at the right side only a very weak capillary wave is formed. The same is noted for $\varphi = 125°$ around $t^* = 17.4$ (not shown here). This is the result of the inclined surface of the liquid film and the subsequent interaction of the left side of the corona with the trailing edge of the solitary wave. Due to these interactions, the expansion of the corona is less pronounced at the left side of the cavity. This results in an earlier merging of the corona with the liquid surface film than at the right side, hence, an earlier formation of the strong capillary waves at the left of the cavity. It is seen that around $t^* - 20.3$ the left side of the cavities for these two wave-phases has changed in shape and the capillary waves have reached the same height as the liquid at the right side of the cavities. Around this non-dimensional time instant the strong capillary waves at the right side of the cavities are formed, after which both capillary waves continue their motion downwards with the same velocity, thereby changing the shape of the cavities at both

sides in the same way as is observed for the impingement onto the steady liquid film, Figure 5.2. Around $t^* = 34.8$ the capillary waves reach the bottom of the cavity and start merging together, Figures 5.5(e) and 5.5(j) and Figures 5.5(d) and 5.5(i).

A completely different receding of the cavity is observed for the wave-phases $\varphi = 1°$, $\varphi = 21°$ and $\varphi = 60°$. For the last of these three wave-phases a single strong capillary wave is formed at the right side of the cavity around $t^* = 17.4$, where the right side of the rim merges with the liquid film. This right capillary wave moves downwards along the surface of the cavity in the next time instants. Since at the left side of the cavity only a very weak capillary wave appears, the receding of the cavity takes place in a strong asymmetrical way. At the right side of the cavity, the shape of the cavity downstream of the capillary wave is changed in a common way - from hemispherical to a straight line - whereas the shape at the left side of the cavity remains almost untouched. This right capillary wave reaches the bottom of the cavity at $t^* = 30.5$, leading to a conical cavity. The vertical symmetry-axis of the cavity has shifted a lot in horizontal position with respect to the point of drop impingement at $t^* = 0$.

Since no corona could be formed at the right side of the cavity for $\varphi = 21°$ and $\varphi = 1°$ due to a direct interaction of this side of the corona with the moving leading edge of the solitary surface wave, it is to be expected that for these impingement phases only at the left side a capillary wave will be formed, which can be seen clearly in the Figures 5.4(f) and 5.4(l). This left capillary wave is preceded by several weak capillary waves, the so-called capillary wave-train. During the subsequent non-dimensional time instants this capillary wave-train moves downwards along the cavity surface, thereby changing the downstream shape at the left side of the cavity, whereas the right side of the cavity remains unchanged and spherical. Around $t^* = 34.8$ and $t^* = 36.8$ the strong left capillary wave reaches the bottom of the cavity for respectively $\varphi = 21°$ and $\varphi = 1°$. At these time instants it is clearly seen that the left side of the cavity has changed its shape to a more or less straight line, hence the common shape for the receding of the cavity upon impingement onto a steady liquid film, whereas the right side of the cavity is still completely hemispherical. Due to this asymmetrical receding of the cavity the inclination of both cavities has increased.

After the capillary waves have reached the bottom of the cavities and, in case of a left and right capillary wave, have merged concentrically, the pressure forces and surface tension forces at the bottom of the cavities become so high that the cavities start to retract. It is observed that, since the capillary waves are created and reach the bottom of the cavity at different non-dimensional times, the time instants of retraction depend also strongly on the phase of the wave upon impingement. The earliest retraction is found for $\varphi = 60°$ at $t^* = 32.9$, since the cavity for this phase is the smallest, hence the capillary wave has reached the bottom of the cavity the earliest.

Although the capillary waves are formed later for $\varphi = 21°$ ($t^* = 20.3$) than for $\varphi = 147°$ ($t^* = 12.3$) and $\varphi = 125°$ ($t^* = 17.4$), the cavities retract for these three phases all at the same time instant $t^* = 36.8$. This is explained by the distances the capillary waves have to travel from the surface of the liquid to the bottom of the cavity. For $\varphi = 21°$ only one strong capillary wave is formed at the left side of the cavity, hence the distance it has to travel to the bottom of the cavity is relatively small. Since for the phases $\varphi = 125°$ and $\varphi = 147°$ the capillary waves are formed earlier, but have to travel a longer way, they reach the bottom of the cavity at approximately the same non-dimensional time instant as for the phase $\varphi = 21°$.

For the phase $\varphi = 1°$ the formation of the capillary wave takes place the latest and the distance it has to travel to the bottom of the cavity is longer than for the phase $\varphi = 21°$, due to which the retraction of the cavity does not start until $t^* = 45.0$.

For all five wave-phases shown here a Worthington jet is formed, but its shape depends strongly on the phase of the solitary surface wave upon impingement. For all the phases it is observed that the jet is not aligned horizontally with the point of impingement, but shifted to a weak or strong amount into the direction of the wave propagation. For $\varphi = 125°$ and $\varphi = 147°$ a small, thick jet appears above the liquid surface, only weakly drifted away from the point of drop impingement. The same short, thick jet is formed for $\varphi = 60°$, but this jet is formed at the outer left side of the recordings, due to the strong asymmetrical receding and retraction of the cavity.

For $\varphi = 1°$ and $\varphi = 21°$ a thick, high jet is formed, for the former one inclined to the right, for the latter one inclined to the left. This difference in inclination of the Worthington jet results directly from the asymmetrical way the cavity retracts.

It can be summarised that the phase of the solitary surface wave on which the drop impinges has a very pronounced effect on the outcome of the impingement process. A clear difference in the prompt splash mechanism and the formation of the corona is present depending on whether the drop impinges onto the leading edge (left directed prompt splash and pronounced corona) or the trailing edge (right directed prompt splash and pronounced corona) of the solitary wave. Both impingement possibilities lead to strong interactions of the corona with the leading edge or trailing edge of the surface wave.

For low wave-phases large cavities are formed, which incline strongly in the direction of the wave propagation, whereas for wave-phases around $\varphi = 60°$ only a small cavity is formed. For wave-phases $\varphi \geq 150°$ the expansion of the cavity is influenced only in a minor way by a difference in wave-phase.

Due to the different corona formation and shape for different wave-phases, the formation and motion of the capillary waves changes magnificently between the different phases. At small phases only a strong left capillary wave is formed, whereas for phases around $\varphi = 60°$ a strong right capillary wave is observed. A capillary wave at both sides of the cavity is found for high wave-phases, whereby the left capillary wave appears before the right one. These differences lead to completely different recedings and retractions of the cavities, as well as different Worthington jets.

### 5.1.3 Influence of impinging drop Weber number on the cavity shape

For each configuration, i.e. phase of the wave at impingement, amplification of the wave and liquid properties, the impingement process for three different Weber numbers of the impinging drop are recorded. The Weber number is changed by changing the value of the terminal velocity of the drop just before impingement. The evolution of the cavity with time is shown in Figure 5.6 for the non-dimensional times inbetween $t^* = -1.5$ and $t^* = 12.3$, in Figure 5.7 and in Figure 5.8 for, respectively, the non-dimensional times from $t^* = 20.3$ to $t^* = 32.9$ and from $t^* = 34.8$ to $t^* = 71.1$. The amplification of the wave, as well as the phase of the wave upon impingement ($\varphi \approx 60°$), are kept the same for all three drop Weber numbers; the liquid for the three cases shown is distilled water.

When comparing the behaviour right after impingement, a few clear differences between the impingement outcomes for the three Weber numbers can be observed. At $t^* = 1.5$ prompt splash is only present for the two higher Weber number; for the lowest Weber number, the kinetic energy of the impinging drop, together with the kinetic energy of the solitary surface

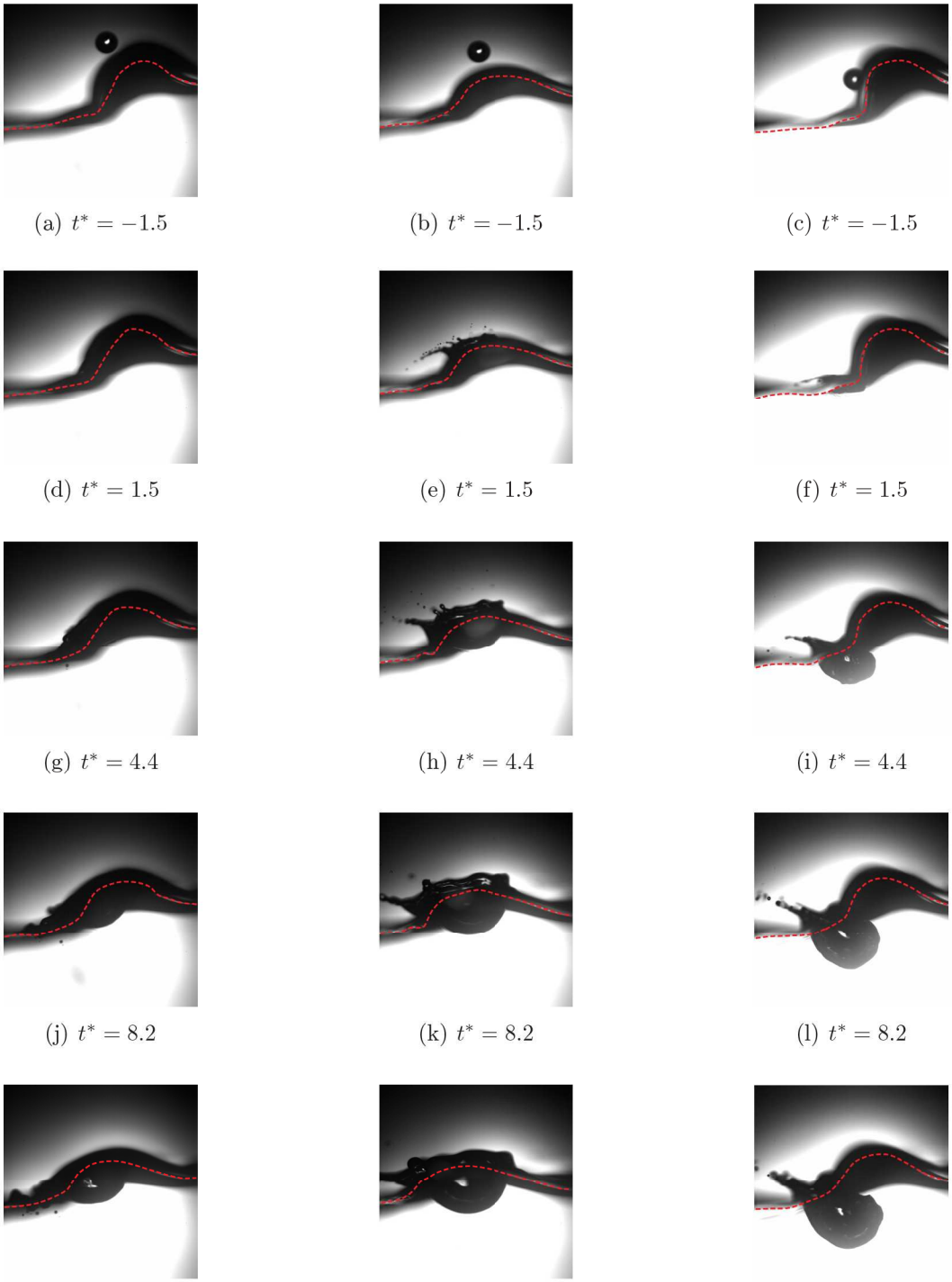

(a) $t^* = -1.5$ (b) $t^* = -1.5$ (c) $t^* = -1.5$

(d) $t^* = 1.5$ (e) $t^* = 1.5$ (f) $t^* = 1.5$

(g) $t^* = 4.4$ (h) $t^* = 4.4$ (i) $t^* = 4.4$

(j) $t^* = 8.2$ (k) $t^* = 8.2$ (l) $t^* = 8.2$

(m) $t^* = 12.3$ (n) $t^* = 12.3$ (o) $t^* = 12.3$

Figure 5.6: Single drop impingement onto a solitary surface wave for different drop impingement Weber numbers. The evolution of the cavity formed by a distilled water drop impingement at non-dimensional time instants between $t^* = -1.5$ and $t^* = 12.3$ The impingement parameters are (left) $D_d = 2.9$ mm, $U_d = 2.7$ m/s, $U_w = 0.4$ m/s and $\varphi = 60°$ ($We = 256$, $Fr = 282$, $Re = 8,552$); (middle) $D_d = 2.9$ mm, $U_d = 3.0$ m/s, $U_w = 0.4$ m/s and $\varphi = 60°$ ($We = 354$, $Fr = 339$, $Re = 10,421$) and (right) $D_d = 2.9$ mm, $U_d = 3.2$ m/s, $U_w = 0.4$ m/s and $\varphi = 56°$ ($We = 400$, $Fr = 391$, $Re = 11,024$)

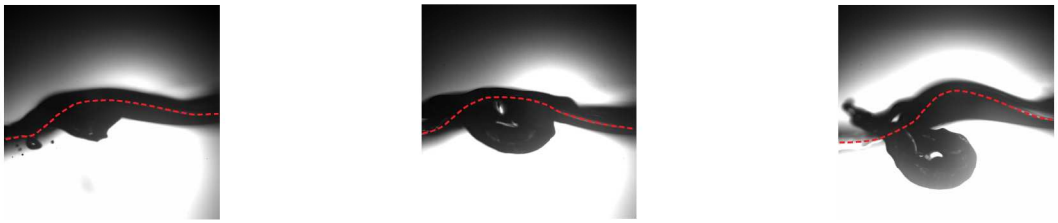

(a) $t^* = 20.3$ (b) $t^* = 20.3$ (c) $t^* = 20.3$

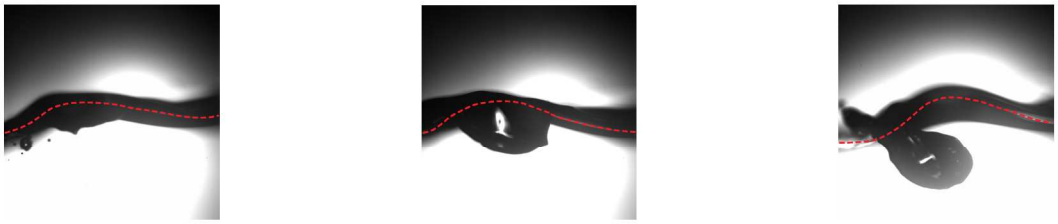

(d) $t^* = 23.2$ (e) $t^* = 23.2$ (f) $t^* = 23.2$

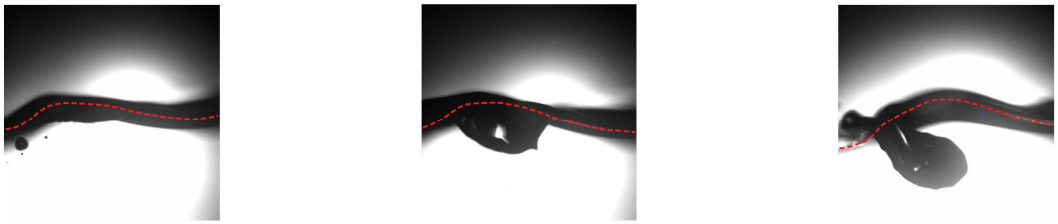

(g) $t^* = 25.6$ (h) $t^* = 25.6$ (i) $t^* = 25.6$

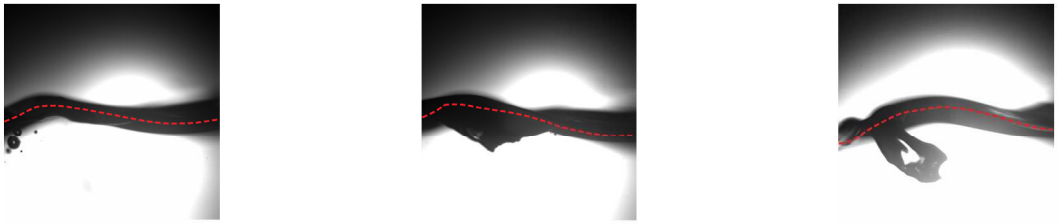

(j) $t^* = 30.5$ (k) $t^* = 30.5$ (l) $t^* = 30.5$

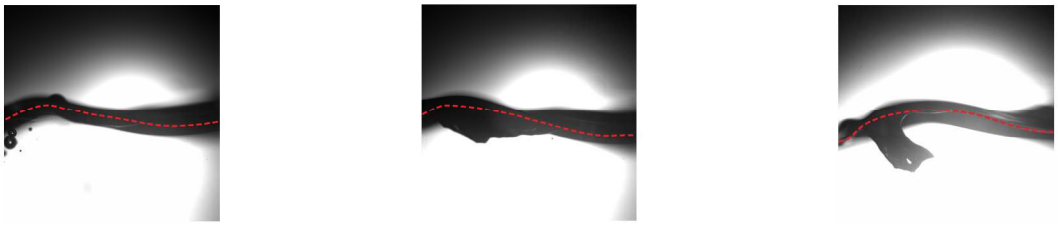

(m) $t^* = 32.9$ (n) $t^* = 32.9$ (o) $t^* = 32.9$

Figure 5.7: Single drop impingement onto a solitary surface wave for different drop impingement Weber numbers. The evolution of the cavity formed by a distilled water drop impingement at non-dimensional time instants between $t^* = 20.3$ and $t^* = 32.9$ The impingement parameters are (left) $D_d = 2.9$ mm, $U_d = 2.7$ m/s, $U_w = 0.4$ m/s and $\varphi = 60°$ ($We = 256$, $Fr = 282$, $Re = 8,552$); (middle) $D_d = 2.9$ mm, $U_d = 3.0$ m/s, $U_w = 0.4$ m/s and $\varphi = 60°$ ($We = 354$, $Fr = 339$, $Re = 10,421$) and (right) $D_d = 2.9$ mm, $U_d = 3.2$ m/s, $U_w = 0.4$ m/s and $\varphi = 56°$ ($We = 400$, $Fr = 391$, $Re = 11,024$)

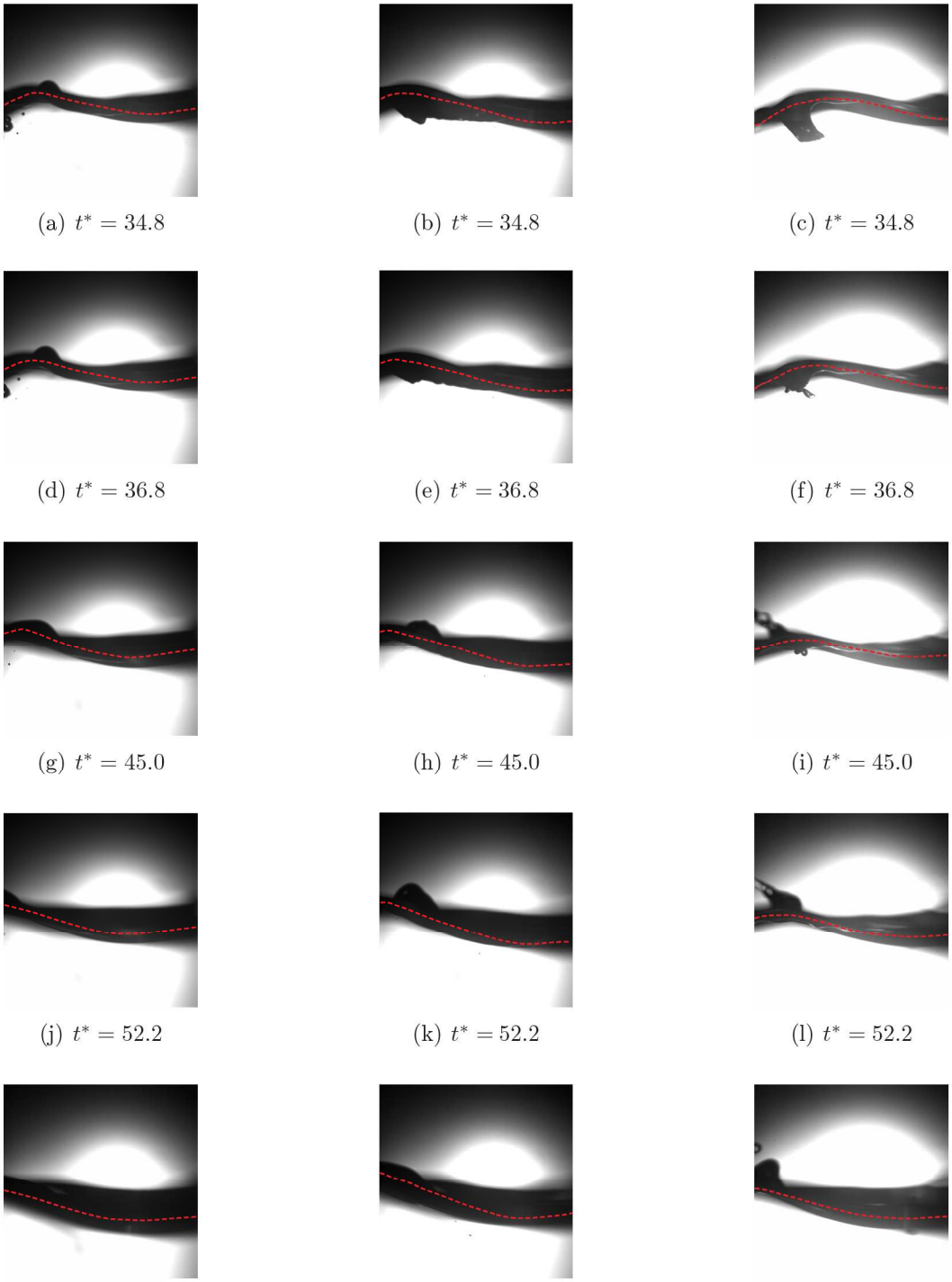

(a) $t^* = 34.8$ (b) $t^* = 34.8$ (c) $t^* = 34.8$

(d) $t^* = 36.8$ (e) $t^* = 36.8$ (f) $t^* = 36.8$

(g) $t^* = 45.0$ (h) $t^* = 45.0$ (i) $t^* = 45.0$

(j) $t^* = 52.2$ (k) $t^* = 52.2$ (l) $t^* = 52.2$

(m) $t^* = 71.1$ (n) $t^* = 71.1$ (o) $t^* = 71.1$

Figure 5.8: Single drop impingement onto a solitary surface wave for different drop impingement Weber numbers. The evolution of the cavity formed by a distilled water drop impingement at non-dimensional time instants between $t^* = 34.8$ and $t^* = 71.1$ The impingement parameters are (left) $D_d = 2.9$ mm, $U_d = 2.7$ m/s, $U_w = 0.4$ m/s and $\varphi = 60°$ ($We = 256$, $Fr = 282$, $Re = 8,552$); (middle) $D_d = 2.9$ mm, $U_d = 3.0$ m/s, $U_w = 0.4$ m/s and $\varphi = 60°$ ($We = 354$, $Fr = 339$, $Re = 10,421$) and (right) $D_d = 2.9$ mm, $U_d = 3.2$ m/s, $U_w = 0.4$ m/s and $\varphi = 56°$ ($We = 400$, $Fr = 391$, $Re = 11,024$)

wave, is not high enough to initiate prompt splash. The value of the cavity diameter depends directly on the impinging drop's Weber number, as the more kinetic energy is present at impingement, the easier the surface tension forces, trying to oppose the expansion of the cavity, can be overcome. This means that at the moment of cavity formation, $t^* \approx 4.4$, the radial expansion of the cavity is smaller for lower Weber numbers. For $We = 256$ almost no cavity has been formed, whereas for $We = 400$ at this non-dimensional time instant a relatively large cavity can be observed. Contrary to the impingement of single drops onto a steady liquid film (§(4.1.3)), the velocity with which the bottom of the cavity penetrates into the liquid film depend strongly on the Weber number of the impinging drop for the impingement onto a solitary wave. The higher the kinetic energy upon impingement is, the more the cavity expands. The corona is seen to be influenced directly by the Weber number as well; for lower Weber numbers, not only a prompt splash is prohibited, but almost no corona is seen to be formed as well. For higher Weber numbers the corona is more pronounced; for $We = 354$ the corona expands the most, but remains stable, whereas for the highest investigated Weber number the corona gets unstable and large jets and secondary droplets are formed at its tip.

As time prolongs the cavity expands further in diameter and depth, whereas at the same time its inclination increases. As has been mentioned before, the inclination of the cavity in the direction of the wave propagation is the direct result of the distribution of the velocity inside the liquid pool. At the surface of the wave the propagation of the liquid is the highest, whereas the liquid velocity decreases for increasing depth. This results in an inclination of the cavity in the direction of wave propagation, which increases in time. Since less kinetic energy of the impinging drop can be converted into surface tension energy and dissipated energy after impingement, the values of the maximum diameter and depth of the cavity are smaller for lower Weber numbers.

Due to the lower corona, the rim falls back sooner onto the liquid film as a result of gravity, leading to an earlier formation of the capillary waves for lower Weber numbers. The strong interaction of the corona with the leading edge of the solitary surface wave leads to the formation of one strong capillary wave at the right side of the cavity. For $We = 256$ this right capillary wave is formed around $t^* = 17.4$ (not shown here), whereas for $We = 354$ this capillary wave appears at $t^* = 20.3$. The subsequent change of the shape of the cavity from hemispherical to conical, due to the influence of the surface tension forces acting on the cavity, starts earlier for the lower Weber number, resulting in an earlier receding of the cavity. The presence of the capillary wave at only one side of the cavity results in an asymmetrical receding of the cavity. At the time instant at which the capillary wave reaches the bottom of the cavity and the subsequent retraction of the cavity starts, $t^* = 21.5$ (not shown here), it is noted that for the cavity of $We = 354$ the capillary wave is still moving downwards. Also here a completely asymmetric receding of the cavity is observed, where during the receding process the shape of the left side of the cavity remains almost unchanged. Only at $t^* = 30.5$, at which the capillary wave reaches the bottom of the cavity, the left side of the cavity is changed drastically from hemispherical to a straight line, before the cavity starts its retracting motion.

The cavity formed at the highest investigated Weber number shows a completely different formation of the capillary waves and subsequent receding. Due to the strong inclination of the cavity at larger non-dimensional times after impingement the right side of the cavity starts to detach from the wave surface, initiating in this way a capillary wave train at this side. Around $t^* = 20.3$ a capillary wave train is also formed at the left side of the cavity. From this time instant on, the receding of the cavity is initiated, as the capillary wave trains start moving downwards along the cavity surface. It is observed that at the top of the cavity its diameter

narrows down in time, whereas at the same moment the inclination of the cavity increases even more. The first phenomenon, the narrowing of the cavity diameter, is the direct result of the surface tension forces, trying to decrease the diameter of the cavity at this point. The increased inclination results from a combination of the velocity difference between the upper and lower layers of the liquid film and the different movements of the capillary waves at both sides of the cavity. These phenomena lead to a completely different receding of the cavity than is observed for the two lower investigated Weber numbers. At the time instant the capillary wave trains reach the bottom of the cavity, the shape of the cavity is not a common cone, but has an approximately inclined cylindrical shape, Figure 5.8(c). The subsequent retraction of the cavity lies around $t^* = 34.8$.

After cavity retraction, a Worthington jet is observed for each of the Weber numbers, but it can be clearly seen that a lower Weber number leads to a thicker jet with a lower maximum height, compare Figure 5.8(d) with Figure 5.8(k). For these two Weber numbers no secondary droplets are observed having pinched-off from the Worthington jet. For the highest Weber number, a thin jet is observed shooting out of the liquid with a relatively high velocity, Figure 5.8(l). This jet is formed with an even larger inclination than is reached maximum by the cavity, as a direct result of the asymmetric retraction of the cavity at $t^* = 36.8$. It cannot be verified whether secondary droplets are being pinched-off, as the Worthington jet for this Weber number continues growing outside of the recordings.

Conclusively, a change in Weber number of the impinging drop has a clear influence on the outcome of the impingement process and on the evolution of the cavity shape in time. A higher Weber number leads to a prompt splash, a higher, larger and unstable corona and a cavity with a larger diameter and depth. The velocity with which the cavity penetrates into the liquid layer depends strongly on the Weber number of the impinging drop. An inclination of the cavity is observed for all investigated Weber numbers, where the angle of inclination and the maximum diameter and depth of the cavity increase sharply for larger Weber numbers

An earlier receding and retraction of the cavity is seen for a lower Weber number, since the kinetic energy of the drop is converted faster into surface tension energy and dissipation energy; hence, the surface tension forces acting on the cavity act sooner. For all the investigated Weber numbers the cavities recede asymmetrically due to the strong capillary wave at the right side of the cavity and the absence or presence of a weak capillary wave at the left side of the cavity.

The Worthington jet that appears after cavity retraction is thicker and reaches a lower maximum height for lower Weber numbers. An inclination of the cavity in combination with a pronounced asymmetric receding of the cavity results in a thin, rapid Worthington jet with an inclination of about 50° with respect to the vertical axis.

### 5.1.4 Influence of the amplification of the solitary surface wave

The velocities and diameters of the impinging drops of the spray change drastically for different positions inside the spray and the kind of spray. For a hollow cone spray the highest impingement velocities can be found at a circle around the impingement center, its diameter depending on the cone of the spray. For a full spray the drops with the highest velocities are found at the center of the spray, as will be shown in Chapter 7. For both sprays the impingement velocities of the spray decrease the further one moves out of the center of the spray. In combination with the increasing diameters of the drops of the spray for larger distances from the center of impingement this leads to strong fluctuations in the velocity and thickness of the surface film

on a local basis.

To investigate the behaviour of the cavity upon impingement onto a solitary wave with various amplitudes, two different amplifications of the solitary surface wave are generated by varying the maximum amplitude of the exciter. As the time in which the exciter moves from its central position to its maximum is kept the same, not only the maximum horizontal motion of the plate that generates these surface waves, Figure 3.2, is changed, thereby changing the maximum amplitude of the solitary wave, but also the velocity with which this solitary wave propagates. This results in two kinds of surface waves; one with a velocity of 0.31 m/s and a maximum amplitude of 2.28 mm - which will be named hereafter "the small wave" -, the other with a velocity of 0.39 m/s and a maximum amplitude of 5.6 mm, the so-called "large wave". These are the wave properties for distilled water; the wave properties for the glycerine/water mixture can be found in Table 3.2.

In this paragraph the evolution of the cavity upon impingement for four of the many investigations done are shown in the Figures 5.9 to 5.11 for the non-dimensional times between $t^* = -1.5$ to $t^* = 71.1$. In each of these figures the time change of the shape of the cavities upon impingement onto two phases of the wave ($\varphi = 60°$ and $\varphi = 149°$) are presented, both for the small and for the large wave. The liquid for the presented impingements is distilled water, the Weber numbers of the impinging drops are around the same value.

The analysis of the data will be split up into two parts, since the differences between the impingements upon $\varphi = 60°$ and upon $\varphi = 149°$ are relatively large. Therefore first of all the results for $\varphi = 60°$ will be discussed, followed by the discussion of the time change of the cavity for $\varphi = 149°$.

At $t^* = 1.5$, right after impingement, a prompt splash is seen to occur for the impingement onto the small wave, leading to many small secondary droplets being pinched-off, Figure 5.9(a). This is followed by the formation and expansion of the corona above the liquid surface and the formation of the cavity below the solitary surface wave. For the large wave, however, no such prompt splash appears and the subsequent formation of the corona is highly asymmetrical. This is the direct result of the strong interaction of the right side of the corona with the leading edge of the large solitary wave, due to which the formation of the corona is prohibited at this side. A small corona is seen to appear at the left side of the cavity, its height and diameter being much smaller than for the impingement onto the small solitary wave, Figure 5.9(j).

As time prolongs the cavity expands symmetrically in radial direction inside the liquid pool for the impingement onto the small wave. It can be seen that the curvature of the wave has almost no influence on the shape and expansion of the cavity, hence the similarity with the expansion of the cavity upon impingement onto a steady liquid pool is large. For the large wave only a small cavity is formed, out of which it can be concluded that much of the kinetic energy is lost upon impingement onto a large amplified wave at a wave-phase of $\varphi = 60°$. The inclination of the cavity in the direction of the wave propagation grows in time for the large wave due to the wave propagation velocity, whereas for the small wave the wave propagation velocity is too small to influence the inclination of the cavity, compare Figure 5.9(q) (small wave) with Figure 5.9(r) (large wave).

Around $t^* = 14.7$ the rims of both cavities fall back onto the liquid surfaces and the capillary waves are formed (not shown here). For the small wave a capillary wave train is formed at both sides of the cavity at almost the same time instant. Both wave trains penetrate into the liquid pool, thereby changing the shape of the cavity in an almost symmetrical way from a hemisphere to an ellipse. Its elliptical shape is reached around $t^* = 27.1$, at which time instant

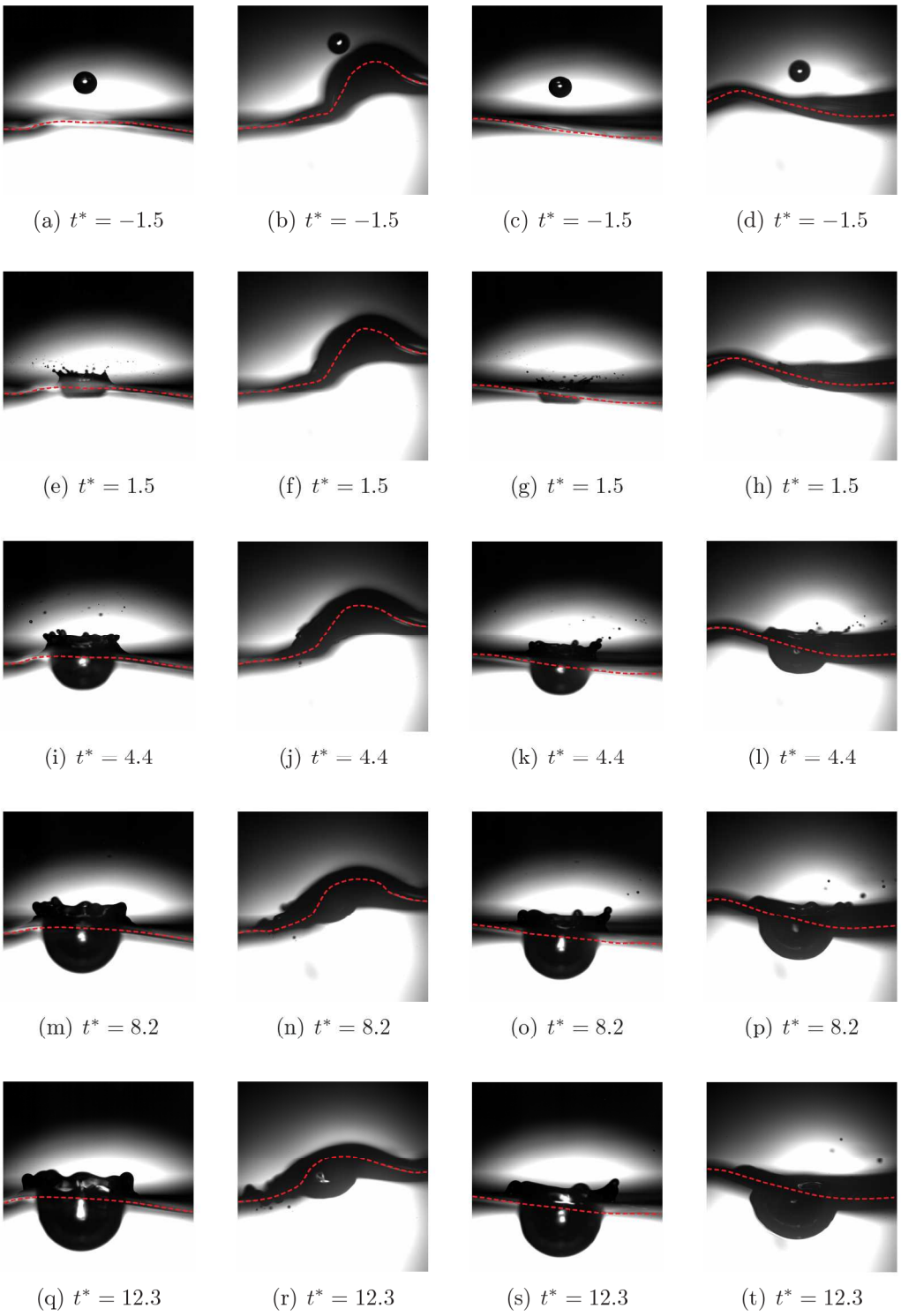

(a) $t^* = -1.5$ (b) $t^* = -1.5$ (c) $t^* = -1.5$ (d) $t^* = -1.5$

(e) $t^* = 1.5$ (f) $t^* = 1.5$ (g) $t^* = 1.5$ (h) $t^* = 1.5$

(i) $t^* = 4.4$ (j) $t^* = 4.4$ (k) $t^* = 4.4$ (l) $t^* = 4.4$

(m) $t^* = 8.2$ (n) $t^* = 8.2$ (o) $t^* = 8.2$ (p) $t^* = 8.2$

(q) $t^* = 12.3$ (r) $t^* = 12.3$ (s) $t^* = 12.3$ (t) $t^* = 12.3$

Figure 5.9: Single drop impingement onto different amplifications of the solitary wave for $\varphi = 60°$ and $\varphi = 149°$. The evolution of the cavity formed by a distilled water drop impingement at non-dimensional time instants between $t^* = -1.5$ and $t^* = 12.3$. The impingement parameters are for all shown phases: $D_d = 2.9$ mm, $U_d = 2.9$ m/s. Outer left: $U_w = 0.3$ m/s and $\varphi = 61°$ ($We = 374$, $Fr = 313$, $Re = 11,080$); Middle left: $U_w = 0.4$ m/s and $\varphi = 60°$ ($We = 256$, $Fr = 282$, $Re = 8,552$); Middle right: $U_w = 0.3$ m/s and $\varphi = 149°$ ($We = 374$, $Fr = 317$, $Re = 11,057$); Outer right: $U_w = 0.4$ m/s and $\varphi = 149°$ ($We = 293$, $Fr = 306$, $Re = 9,291$)

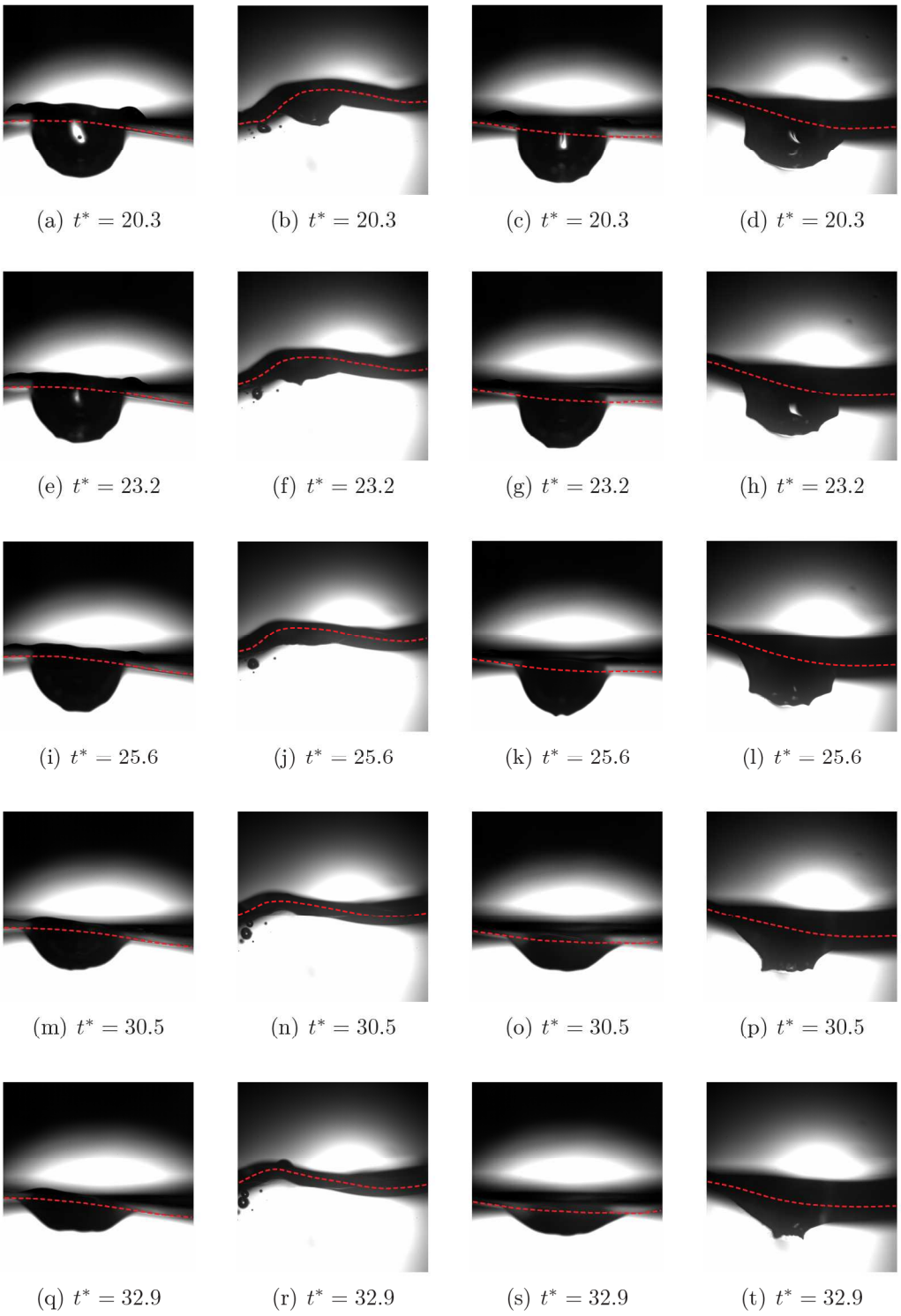

(a) $t^* = 20.3$ (b) $t^* = 20.3$ (c) $t^* = 20.3$ (d) $t^* = 20.3$

(e) $t^* = 23.2$ (f) $t^* = 23.2$ (g) $t^* = 23.2$ (h) $t^* = 23.2$

(i) $t^* = 25.6$ (j) $t^* = 25.6$ (k) $t^* = 25.6$ (l) $t^* = 25.6$

(m) $t^* = 30.5$ (n) $t^* = 30.5$ (o) $t^* = 30.5$ (p) $t^* = 30.5$

(q) $t^* = 32.9$ (r) $t^* = 32.9$ (s) $t^* = 32.9$ (t) $t^* = 32.9$

Figure 5.10: Single drop impingement onto different amplifications of the solitary wave for $\varphi = 60°$ and $\varphi = 149°$. The evolution of the cavity formed by a distilled water drop impingement at non-dimensional time instants between $t^* = 20.3$ and $t^* = 32.9$. The impingement parameters are for all shown phases: $D_d = 2.9$ mm, $U_d = 2.9$ m/s. Outer left: $U_w = 0.3$ m/s and $\varphi = 61°$ ($We = 374$, $Fr = 313$, $Re = 11,080$); Middle left: $U_w = 0.4$ m/s and $\varphi = 60°$ ($We = 256$, $Fr = 282$, $Re = 8,552$); Middle right: $U_w = 0.3$ m/s and $\varphi = 149°$ ($We = 374$, $Fr = 317$, $Re = 11,057$); Outer right: $U_w = 0.4$ m/s and $\varphi = 149°$ ($We = 293$, $Fr = 306$, $Re = 9,291$)

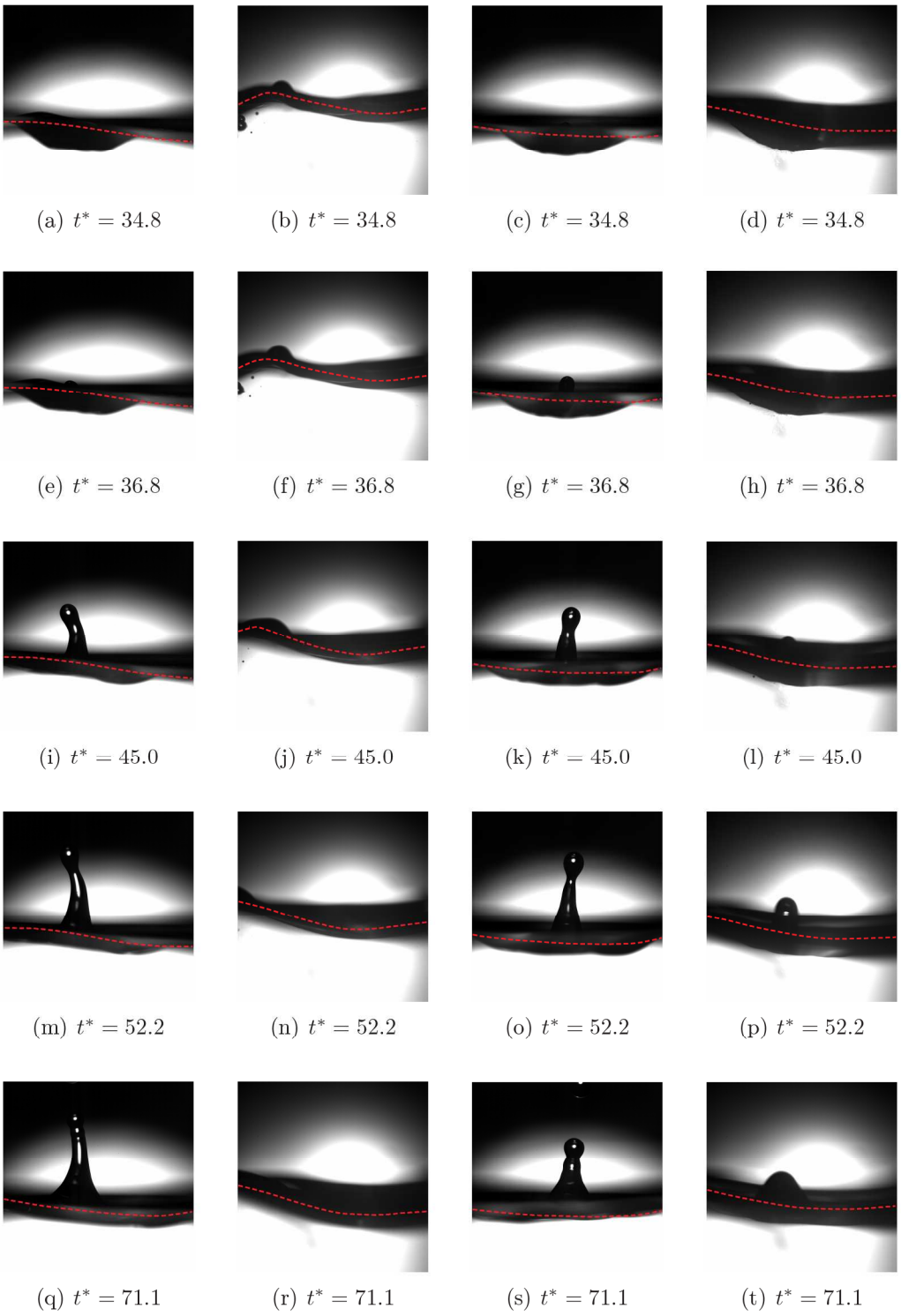

(a) $t^* = 34.8$ (b) $t^* = 34.8$ (c) $t^* = 34.8$ (d) $t^* = 34.8$

(e) $t^* = 36.8$ (f) $t^* = 36.8$ (g) $t^* = 36.8$ (h) $t^* = 36.8$

(i) $t^* = 45.0$ (j) $t^* = 45.0$ (k) $t^* = 45.0$ (l) $t^* = 45.0$

(m) $t^* = 52.2$ (n) $t^* = 52.2$ (o) $t^* = 52.2$ (p) $t^* = 52.2$

(q) $t^* = 71.1$ (r) $t^* = 71.1$ (s) $t^* = 71.1$ (t) $t^* = 71.1$

Figure 5.11: Single drop impingement onto different amplifications of the solitary wave for $\varphi = 60°$ and $\varphi = 149°$. The evolution of the cavity formed by a distilled water drop impingement at non-dimensional time instants between $t^* = 34.8$ and $t^* = 71.1$. The impingement parameters are for all shown phases: $D_d = 2.9$ mm, $U_d = 2.9$ m/s. Outer left: $U_w = 0.3$ m/s and $\varphi = 61°$ ($We = 374$, $Fr = 313$, $Re = 11,080$); Middle left: $U_w = 0.4$ m/s and $\varphi = 60°$ ($We = 256$, $Fr = 282$, $Re = 8,552$); Middle right: $U_w = 0.3$ m/s and $\varphi = 149°$ ($We = 374$, $Fr = 317$, $Re = 11,057$); Outer right: $U_w = 0.4$ m/s and $\varphi = 149°$ ($We = 293$, $Fr = 306$, $Re = 9,291$)

the capillary wave trains have reached the bottom of the cavity and the retracting motion of the cavity begins. Only one large capillary wave is formed for the large wave at the right side of the cavity, thereby changing the shape of the cavity in a strong asymmetrical way. The left side of the cavity remains hemispherical during the receding phase, whereas the right side of the cavity changes from hemispherical to a straight line. Since the cavity for the large wave is relatively small, the right capillary wave reaches the bottom of the cavity already after a few non-dimensional time instants. From this time instant on ($t^* = 23.3$) the cavity starts its retracting motion, driven by the surface tension and high pressures at the bottom of the cavity, Figure 5.10(e).

For both impingements a Worthington jet is formed, although being completely different in shape and size. For the small wave a thin high jet is formed, positioned approximately at the same position at which the drop impinged. This central jet is slightly curved as the result of the slightly asymmetrical retraction of the cavity. For larger times the central jet erects and some secondary drops are formed at its top. Only a small, thick jet is formed for the impingement upon the large wave. This is explained by the small size of the cavity, resulting in small surface tension forces, in combination with the highly asymmetrical receding and retraction of the cavity. This leads to a jet that has shifted a lot in horizontal position with respect to the impingement position of the drop.

The second part of the comparison between the time evolution of the cavity upon impingement onto a small and onto a large solitary surface wave concerns the drop impingement onto the wave-phase $\varphi = 149°$. At this phase, the highest amplitude of the waves has passed already the impingement point, hence the shape of the surface is declining seen from the left of the recordings.

First of all, it has to be noticed that the time change of the cavity shapes for the impingements onto the small wave are almost identical for both wave-phases. Small differences in the position of the capillary waves at the same time instants after impingement can be observed, leading to small differences in the way the cavity recedes and retracts. This, in turn, results in a central jet for $\varphi = 149°$ that is inclined to the right, instead of to the left, as is seen for $\varphi = 61°$, compare Figure 5.11(m) with Figure 5.11(o). This leads to the conclusion that the amplitude and velocity of the small solitary surface wave are too small to provoke large differences in the shape of the cavity for different wave-phases, although it can be observed that the inclination of the jet correlates with the inclination of the wave surface.

When comparing the impingement processes between the two waves for $\varphi = 149°$ it is observed that for both waves a pronounced prompt splash occurs right after impingement ($t^* = 1.5$). The surface of the liquid pool is inclined twice as much for the larger wave, due to which in this case a stronger interaction of the left side of the corona with the trailing edge of the wave occurs. This interaction is not so pronounced for the small wave, resulting in a symmetrical expansion of the corona, whereas for the large wave the expansion of the left side of the corona is prohibited by the presence of the wave surface.

Both cavities expand in radial direction with time, until the instant at which all the kinetic energy, present upon impingement, is converted into surface tension energy and dissipated energy. At this time instant the cavity for the smaller wave has penetrated deeper into the liquid pool, although its diameter is smaller compared to the larger wave. The inclination of the cavities is relatively small, hence the velocity of the surface wave has only little influence on the shape of the cavity for higher wave-phases at impingement. At about the same time, $t^* = 12.3$, the capillary waves are formed. For the smaller wave an almost symmetric capillary wave-train is formed at both sides of the cavity, whereas for the larger wave a strong capillary wave is